Materials and Design 196 (2020) 109155

Contents lists available at ScienceDirect

Materials and Design

journal homepage: www.elsevier.com/locate/matdes

Topological and morphological design of additively-manufacturable spatially-varying periodic cellular solids

Ali Y. Tamijani *, Shajayra Patricia Velasco, Lee Alacoque

Aerospace Engineering Department, Embry-Riddle Aeronautical University, Daytona Beach, Florida 32114, United States of America

HIGHLIGHTS

- A framework is created to generate microstructures that are tailored to attain the macrostructure's optimized performance
- The framework can be used with any types of cells and lattices due to the use of spatial harmonics decomposition
- The implementation of multiple load cases demonstrates the applicability of various types of cells and lattices
- The experimental tests of the optimized cellular solids show significant improvement in stiffness and strength

GRAPHICAL ABSTRACT

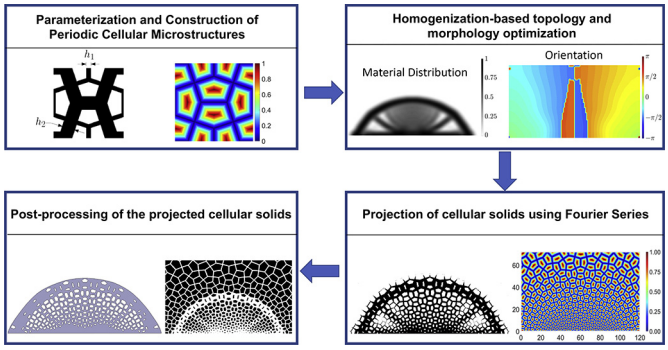

ARTICLE INFO

Article history:
Received 8 July 2020
Received in revised form 2 September 2020
Accepted 14 September 2020
Available online 16 September 2020

Keywords:
Topology optimization
Morphology optimization
Cellular solids
Lattice structures
Additive manufacturing

ABSTRACT

The focus of this research is to create a methodology to systematically generate spatially-varying, periodic, cellular microstructures that are tailored to attain optimized performance of the macrostructure. The unit cell lattice is represented by Fourier series expansions, and the corresponding amplitudes and phase spectrum are obtained. Then, the material distribution (topology) and orientation of each cell (morphology) are optimized for multiple load cases. The phase of the spatial harmonics is updated based on the optimized orientation, and the analog response is thresholded with the optimized material distribution to find the binary lattices. The framework is tested for three types of lattices with various periodicities. The square cell with a rectangular hole shows the exploitation of the cell's orthotropic properties for structures subjected to a single load case; the triangular cell with the triangular lattice depicts the applicability of other types of cells and lattices to transfer shear for the structures subjected to multiple load cases; and the square cell with pentagonal lattices shows the versatility of the framework. An optimized triangular cellular solid is additively manufactured, and it is validated experimentally that 12% higher stiffness and 57% higher strength can be achieved compared to the conventional topology optimization design.

1. Introduction

A cellular solid is comprised of an assembly of full materials and voids (binary microstructures). In nature, cellular solids are found in trabecular bone, wood, cork, and plant parenchyma [1]. Inspired by nature, cellular solids have been utilized in various applications [2], including 1) efficient lightweight structures due to their high stiffness and strength-to-weight ratio [3]; biomedical applications due to their controllable cells and stiffness [4]; heat exchangers and cooling machines due to their large surface area and low flow resistivity [5]; energy absorbers due to their capability of sustaining large deformations [6]; and acoustic insulation due to their porosity [7].

* Corresponding author.
E-mail addresses: tamijana@erau.edu (A.Y. Tamijani), velascos@my.erau.edu (S.P. Velasco), alacoqul@my.erau.edu (L. Alacoque).

https://doi.org/10.1016/j.matdes.2020.109155

Periodic cellular solids are multiscale problems in which the performance of the macrostructure is derived by the effective properties and, hence, the micro-architectures of cellular solids. Thus, the structural performance can be optimized by designing spatially-varying architectures of local cells, including their amounts of material, their orientations, and their sizes. Topology optimization can be utilized to optimize the distribution of the material. Topology optimization inherently is a binary design optimization in which the design variable, material distribution, is one for solid or zero for void. The binary design field can be relaxed by utilizing the homogenized macroscopic properties of microstructures and implementing the gradients of the objective and constraints in the optimization process [8–10]. The orientations of the cells are obtained using Pedersen strain-based [11] or stress-based methods [12]. Both methods use the compliance of the design as the objective function. In the stress method, stress is assumed fixed with respect to the orientation of the cell, while, in the strain-based method, the strain field is considered to be fixed. Homogenization-based topology optimization results in "gray" regions, which represent infinitely small microstructures. Later, this method was extended to maximize the macrostructure performance with an optimization of the microstructure using inverse homogenization through a hierarchical computational scheme [13]. Due to the high computational cost of performing finite element analysis on such complex, small-scale structures, homogenized material properties can be used as a surrogate model in a macroscale optimization to reduce this cost. However, in a homogenization-based multiscale approach, the connectivity of microstructures between surrounding cells is not considered. The lack of connectivity of spatially varying cellular solids in fabricated artifacts results in a large difference between predicted and measured performance. Homogenization-based optimization also is based on infinite periodicity, which results in periodic cells consisting of infinitesimal features. However, fabrication of the cellular structure requires a scale with a finite length. Zhang, Gao, and Xiao [14] addressed the connectivity between microstructures by a kinematical connective constraint. In their study the optimized design of multiple prototype microstructures is obtained by using a homogenization-based level set method. Then the level set functions are interpolated to generate a set of microstructures to construct a Kriging metamodel, and the material distribution is optimized for maximizing the natural frequency of the cellular structures. This method was later applied to multiscale topology optimization of sandwich structures with graded cellular cores [15].

Another approach to ensure the connectivity of microstructures is the post-treatment of the homogenization-based topology optimization which first was reported by Pantz and Trabelsi [16]. A rank-two laminate is used in the optimization process, but due to the issue concerning its manufacturability, square cells with rectangular holes were used in the construction of the optimized design on a fine mesh. A coherent orientation was required to establish the optimization of the lattice structures, but the orientation was symmetric with respect to π. To resolve this issue, Pantz and Trabelsi [16] obtained a mapping function by solving a least squares minimization with several constraints to remove the sudden changes in the orientation. Later, Groen and Sigmund [17] simplified the procedure used to obtain the mapping function for the square cells with rectangular holes by using the connected component labeling method and by including a relaxation coefficient in the least squares minimization. They also implemented a scaling factor based on average lattice spacing to better control the size of the unit cell in the optimized design. Recently, Allaire, Geoffroy-Donders, & Pantz [18] addressed the discontinuity in the orientation by substituting an abstract manifold for the computational domain and imposing the conformality condition. In their work, the exponential of a dilation field also was considered in the process of establishing the mapping function to preserve the geometric properties of the cell.

The focus of the research mentioned above was on a square cell with a rectangular hole subjected to a single load case. The objective of this research is to extend the de-homogenization approach and create a methodology to systematically generate optimized, spatially-varying, manufacturable, periodic cellular solids that can be applied to different types of cells and lattices and subjected to multiple load cases. The cellular structures in this research consist of 2D cell types replicated in the out-of-plane direction. The lattices are the binary microstructures within the cell. It has been shown in crystallography that various periodic cellular solids can be created using Fourier series [19]. Rumpf and Pazos [20] also showed that a distance function can be used to establish the Fourier series and that a mapping function can be used to develop spatially-varying, periodic cellular solids. Thus, to obtain the topological and morphological design of spatially-varying cellular structures, the periodic cellular solids are represented using spatial harmonics. Subsequently, the topology optimization is performed by utilizing the effective properties obtained by numerical homogenization. The homogenization-based optimization is based on infinite periodicity and yields infinitesimally disconnected cellular microstructures. In order to establish interconnected microstructures, the spatial harmonics are reconstructed using their shape-preserving phases. Then, manufacturing constraints are incorporated in the reconstruction and the post-treatment process by using the periodicity of the lattice.

The framework developed in this research consists of four steps, i.e., [1] Parametrization and Construction of Periodic Cellular Microstructures: In this step, the characterizing parameters required to generate the lattice geometry are identified, the phase spectrum and amplitude to establish the Fourier series are calculated, and a database is developed for the homogenized properties for various characterizing parameters; [2] Homogenization-Based Topology Optimization: In this step, the optimization problem to find the optimized cell morphology and material distribution subjected to multiple load cases is established; [3] Projection of cellular solids using Fourier series: The optimized orientation is regularized, the mapping functions that correspond to the phase of the spatial harmonics are developed, and the analog and binary lattices are obtained; [4] Post-processing of projected cellular solids: In this step, the projected cellular solids are modified based on the feature periodicity, cell porosity, and minimum manufacturable feature size; the floating members are identified and removed, and the boundary of the cellular solid is smoothed. The four major contributions of the current research are as follows; (a) While two types of cells and three types of lattices, i.e., square cell with rectangular hole, triangular cell with triangular lattice, and square cell with pentagonal lattices, were selected to convey the ideas in this research, due to the versatile spatial harmonics decomposition, the proposed framework can be used with any types of cells and lattices; (b) the implementation of multiple load cases demonstrates the applicability of various types of lattices; (c) the manufacturing post-treatment process can identify both small thicknesses and small holes for various type of cells and lattices and produce a design that can be additively manufactured; (d) the optimized cellular solids and those obtained using Solid Isotropic Material with Penalization (SIMP) are manufactured additively, and it is validated experimentally that the stiffness is improved by using the optimized cellular structures and that significantly higher strength is achieved due to the redundant load paths provided by the cellular solids.

2. Parameterization and construction of periodic cellular microstructures

The first step in the generation of a cellular solid is to select the types of cells and lattices, such as square cells with rectangular holes, triangular cells with triangular lattices, or square cells with pentagonal lattices. Then, the parameters that correspond to the evolution of a unit cell geometry must be selected. For example, Fig. 1 shows the characterizing parameters for square, triangular, and pentagonal lattices. One parameter or multiple parameters (i.e. , h_n, where n is the number of parameters) can be selected to control the geometry of the lattice within the

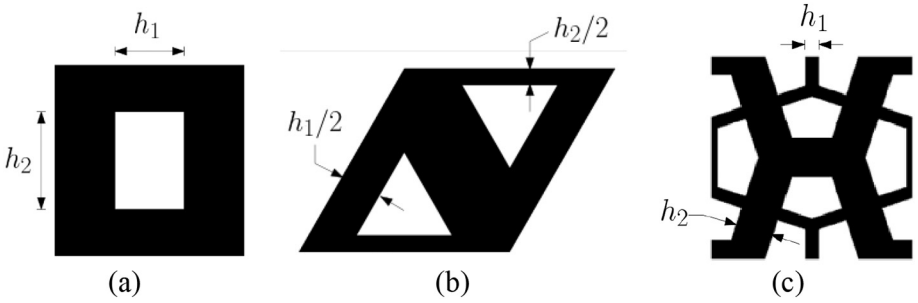

Fig. 1. Parametrization: (a) for a square lattice with a rectangular hole; (b) for a triangular lattice; (c) for a Cairo pentagonal lattice

cell. For example, each cell in Fig. 1 contains two parameters to develop the geometry of the lattice. Alternatively, each cell could have one parameter (e.g., $h_1 = h_2$). The parameters also can be related to the void (Fig. 1 (a)), or the solid thickness (Fig. 1 (b) and (c)). The parameters are normalized between 0 and 1. The parameters do not necessarily show the thickness of the lattice. For a square with a rectangular hole lattice, the thickness is $t_n = 1 - h_n$, and for the triangular lattice, the thickness of the members are $t_n \approx \sqrt{3}/2h_n$, while they are $t_n \approx 1/\sqrt{8}h_n$ for the pentagonal lattice.

The selection of the parameter has a significant effect on the mechanical properties. Generally, a larger design space is allowed when the number of parameters is increased, which provides better control of the local mechanical properties. For example, while the triangular lattice with a single parameter for thickness has isotropic properties, the selection of two parameters results in anisotropic properties. Fig. 2 shows the polar plots of homogenized stiffness for various lattices. As can be seen, there is a larger homogenized Young's modulus in the directions parallel to the walls of the square that has a rectangular hole and triangular lattices, and the best shearing stiffness occurs 1) in the 45 degree angle for the square cell with a rectangular hole, and 2) in the vertical and horizontal directions for the triangular lattice (Fig. 2 (a) and (b)). These types of anisotropic properties provide the opportunity to design the orientation of the local cell with respect to the applied loads, and, as a result, obtain more efficient macrostructures. While there is orthotropy for the low parameter values of the Cairo pentagonal lattice, it diminishes quickly.

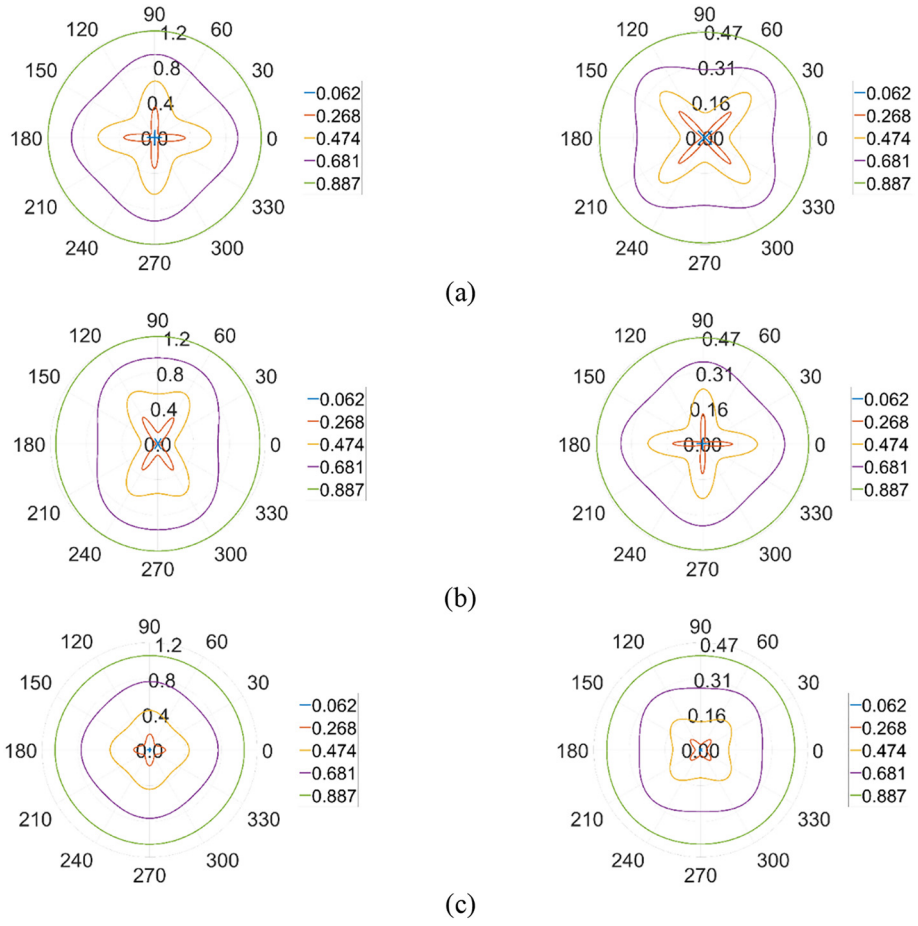

Fig. 2. Polar plots of homogenized Young's modulus and shear modulus of: (a) square with rectangular hole lattice; (b) triangular lattice (c) Cairo pentagonal lattice for different values of h_1

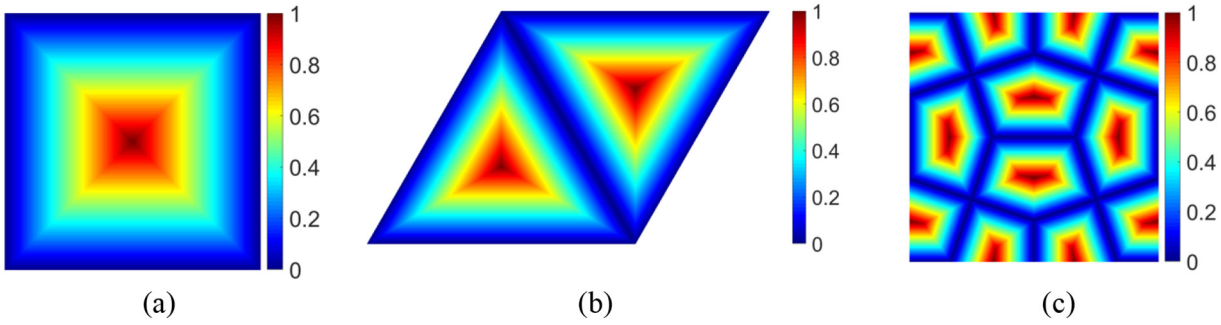

Fig. 3. Distance functions: (a) square cell with rectangular hole; (b) triangular lattice; (c) Cairo pentagonal lattice

Next, the unit cell configuration is constructed using a distance function, i.e., $d_n(x,y,z)$, where $d_n(x,y,z) \le h_n$ is solid and $d_n(x,y,z) > h_n$ is void. (If h_n is related to the void thickness, then $1 - h_n$ is utilizEd.) Assuming that $h_1 = h_2$, Fig. 3 shows the distance functions that correspond to the various lattices.

Since the cellular solid is created by the periodic repetition of a unit cell, $d_n(x,y,z)$ can be decomposed into spatial harmonics and represented using a Fourier series. To this end, the periodic lattice vector concept for crystal structures [19,20] is borrowed to generate cellular solids. In crystallography, a crystal structure consists of a periodic array of structural units. Each unit cell is considered as an imaginary point; hence, the cellular solid (Fig. 4 (a)) becomes an array of equivalent points called the points of lattice. (See Fig. 4 (b).) Five unique point lattice arrays exist in 2D, i.e., oblique, rectangular, square, triangular, and rhombus arrays [19]. To connect two different points in the points of lattice, the primitive lattice vectors $\boldsymbol{a}_1$ and $\boldsymbol{a}_2$ (Fig. 5 (a) and (b)) are introduced, where Λ is the spacing between successive points of lattice in the direction of the primitive lattice vectors. In order to repeat the lattices infinitely on a 2D space, wave vectors are introduced that are referred to as the reciprocal lattice vectors, $\boldsymbol{G}_{pq}$ [19] (see Fig. 5 (c) and (d):

$$\mathbf{G}_{pq} = p\mathbf{G}_1 + q\mathbf{G}_2$$

$$\mathbf{G}_1 = 2\pi \frac{\boldsymbol{a}_2 \times \hat{z}}{\boldsymbol{a}_1 \cdot (\boldsymbol{a}_2 \times \hat{\mathbf{z}})} \quad \mathbf{G}_2 = 2\pi \frac{\hat{z} \times \boldsymbol{a}_1}{\boldsymbol{a}_1 \cdot (\boldsymbol{a}_2 \times \hat{\mathbf{z}})} \tag{1}$$

where $\hat{\boldsymbol{z}}$ is the perpendicular axis to the 2D plane, and p and q are integers. A special characteristic of the reciprocal vectors is that the waves that propagate along these directions have the same periodicity as the points of lattice, which implies that $exp(j\boldsymbol{G}_{pq} \cdot \boldsymbol{r}) = exp\,(j\boldsymbol{G}_{pq} \cdot (\boldsymbol{r} + \boldsymbol{R}))$, where $\boldsymbol{r}$ is the position vector, and $\boldsymbol{R}$ is the vector to create the points of lattice [19]. Thus, the reciprocal lattice vector shows the orientation of periodicity, and its magnitude is the inverse of the spatial period between the successive points of the lattice. By using the periodicity characteristic of the reciprocal lattice vector, the cellular solid is expressed using a complex Fourier series [19]:

$$\psi_n = \mathrm{Re}\left(\sum_p \sum_q b_{pq}^n e^{j\mathbf{G}_{pq}\cdot\mathbf{r}/\Lambda}\right) \tag{2}$$

where b_{pq}^n is the amplitude of the pq^{th} harmonic, which is obtained by the Fourier transform of the distance function (d_n) that is used to generate the geometry of the lattices. The Fourier transform moves the lattice from the spatial domain to the frequency domain considering a limited, but large enough, group of frequencies. It is good practice to shift the highest frequencies to the center cell domain, and since the significant terms are located in the center, a truncated Fourier transform is generated by considering a window of amplitudes around the center [20]. Therefore, the truncated amplitude and reciprocal lattice vector (b_{pq}^n and $\boldsymbol{G}_{pq}^n$) are obtained for each parameter.

Next, a database of density (ρ) as a function of cell parameters was constructed while keeping the reciprocal vectors unchanged (see Fig. 6 (a)). The database for the homogenized properties also was constructed using the parameters of the cells. The homogenized mechanical properties of periodic cellular solids were obtained using numerical homogenization [21–23] over a finite element mesh of cell domain Y created by [$\boldsymbol{a_1}$, $\boldsymbol{a_2}$]:

$$\int_Y C_{ijpq}\left(\frac{\partial \chi_p^{kl}}{dy_q} - \varepsilon_{pq}^{(0)kl}\right)\frac{\partial v_i}{\partial y_j}\,dY = 0$$

$$C_{ijkl}^H(r) = \frac{1}{|Y|}\int_Y C_{mspq}(r,y)\left(\varepsilon_{pq}^{(0)kl} - \varepsilon_{pq}\left(\chi^{kl}\right)\right)\left(\varepsilon_{ms}^{(0)ij} - \varepsilon_{ms}\left(\chi^{ij}\right)\right)dY \tag{3}$$

where $\boldsymbol{\varepsilon}^{(0)kl}$ are the three macroscopic unit strains, $\boldsymbol{\chi}^{kl}$ are the displacement fields, v_i is the virtual displacement field, and $\boldsymbol{C}$ is the stiffness tensor of the cell material. As demonstrated in Fig. 6 (b), the homogenized

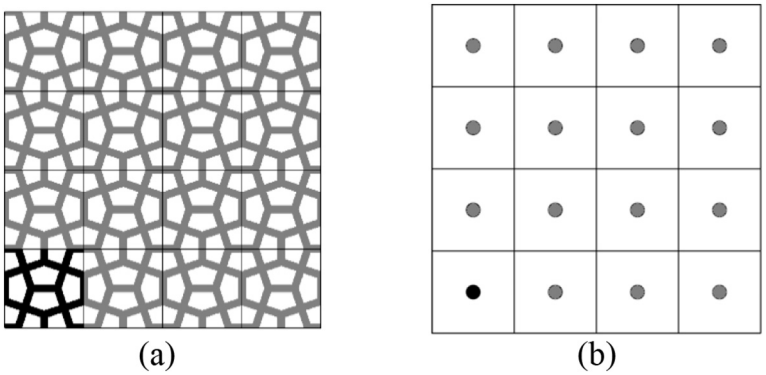

Fig. 4. (a) 4x4 Cairo pentagonal lattice; (b) point lattice replacing the Cairo pentagonal cell

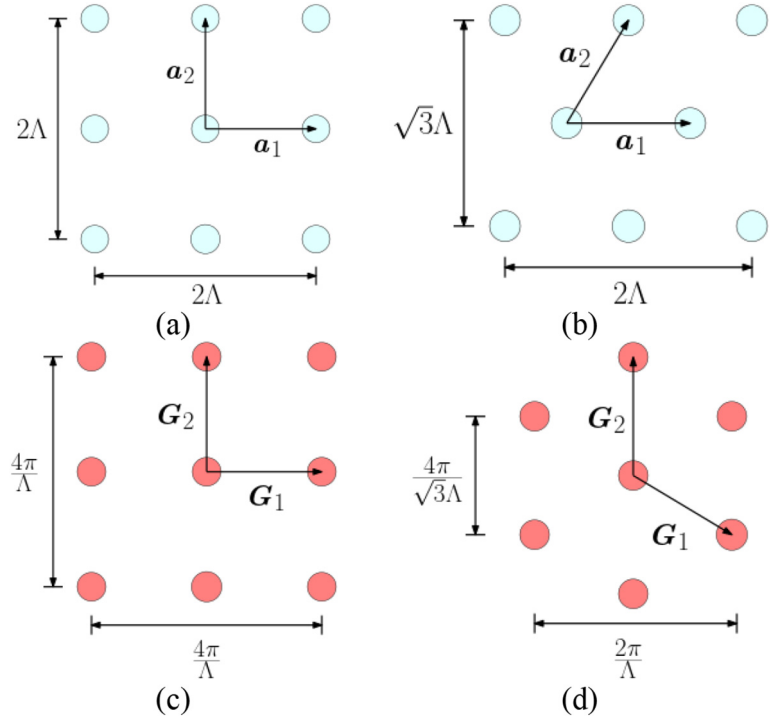

Fig. 5. Primitive lattice vectors (a) for the square unit cell; (b) for the triangular unit cell; reciprocal lattice vectors for (c) the square unit cell; and (d) triangular unit cell [19]

properties were obtained for various cell parameters to construct a response surface, $\boldsymbol{C}^H(h_n)$.

The response surfaces related to the density and elasticity tensor were generated once, and they were used within the homogenization-based topology optimization. However, the homogenized properties were obtained based on the assumption of infinite periodicity, and it is important to investigate the convergence of the effective properties to the homogenized properties of the cellular solids numerically with a finite cell number; also, it is important to validate the numerical model experimentally. Thus, a finite element analysis (FEA) was performed according to the method used by Maskery et al. [24] to measure the effective elastic modulus for cellular solids with various numbers of cells and different types of lattices. A displacement in the vertical direction was prescribed to the top surface to compress the structure in the in-plane direction. On the bottom surface, the displacement was constrained only in the vertical direction. A single node on a corner of the bottom surface was constrained fully to prevent the rigid body translation. These boundary conditions compressed the structure while allowing the top and bottom surfaces to expand freely. The effective elastic modulus was obtained from Eq. (4):

$$E^* = \frac{FL}{A\delta} \tag{4}$$

where δ is the prescribed displacement, F is the reaction force produced by the prescribed displacement, A is the cross-sectional area of the structure, and L is the undeformed height of the structure. Cellular solids that had 30% relative density and up to 8 repetitions in each direction were analyzed. Fig. 7 is a plot of the normalized results, and it shows the different behaviors of each of the cell geometries as their effective stiffnesses converged to their homogenized values. With the compression load applied parallel to the cell walls in the square cell with a rectangular hole, the effective elastic modulus has no dependence on the number of cells and is always equal to the result of homogenization. This behavior is a result of the load being perfectly parallel to the vertical members. For spatially varying optimized square cells with rectangular holes where the orientations of the cells are aligned with the load paths of a single load case, there should be little dependence of the stiffness of

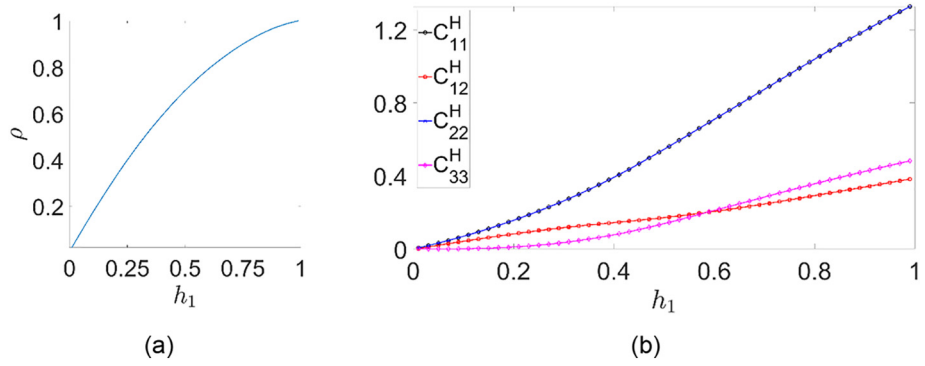

Fig. 6. (a) Cairo pentagonal density; (b) Cairo pentagonal homogenized mechanical properties

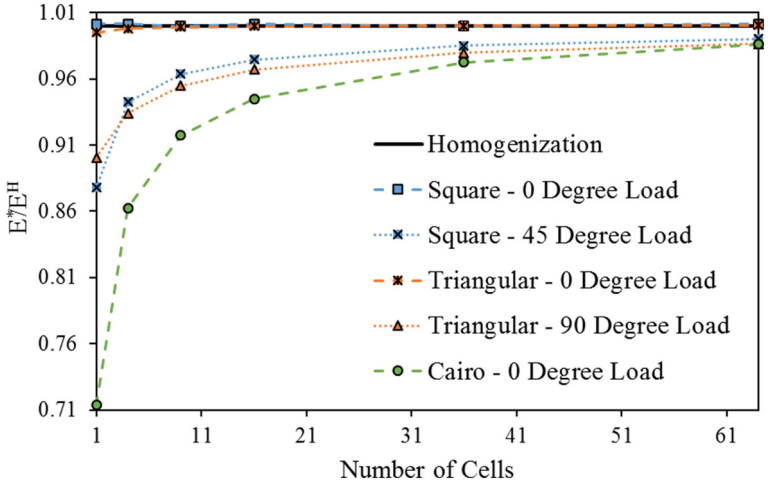

Fig. 7. Normalized effective Young's modulus versus the number of cells that made up the cellular solids; the normalized homogenized values are shown by the solid black horizontal line

the structure on the number of cells that comprise it. When the square lattice is loaded diagonally at a 45-degree angle, the effective Young's modulus was dependent on the number of cells since now the deformation is dominated by bending. Similarly, the triangular lattice with the load applied in the 90-degree direction starts at a lower stiffness that converges up to the homogenized value. When the load is applied in the 0 degree direction, which is parallel to one of the three directions of the wall, it behaves similarly to the square lattice, and just a single cell is very close to the homogenized value. For the Cairo pentagonal lattice, there are no continuous members, so deformation always is dominated by bending, and convergence of the stiffness with the number of cells occurs for a load applied in any direction. The results of this analysis point to the conclusion that the assumptions of homogenization theory, in which the unit cells are significantly smaller than the macrostructure, are not restrictive to the macro cellular solids presented in this article. With a 3×3 grid of unit cells (a periodicity of 1/3), each of the three different lattices analyzed here had stiffness values within 90% of the homogenization values.

Next, the FEA results were compared to the experimental tests. Six specimens for two lattice types, i.e., a square cell with a rectangular hole and a Cairo pentagonal, were additively manufactured in 3×3 configurations at 30% relative density. The specimens were fabricated using Multi Jet Fusion with thermoplastic polyamide 12 (PA12) material. In the Multi jJet Fusion process the fusing and detailing agents are applied to the powder bed and an infrared heater moves over the bed to fuse the layer. The specimens were scaled such that the wall thicknesses were approximately 2mm. They were tested under compression in a universal testing machine with a 50*kN* load cell. The material properties of PA 12 were tested from coupons additively manufactured by Multi Jet Fusion, and the elastic modulus and Poisson's ratio were found ($E =$ 1260MPa, and $\nu = 0.3$). The experimental results of the stiffness summarized in Table 1 confirmed that only three repetitions of the unit cells achieved stiffness values that were within 90% of the homogenization value.

Table 1
3×3 base cell additively-manufactured test specimens loaded in the vertical direction

E^*/E^H	Square	Cairo
Homogenization (Plane Stress)	1.00	1.00
Standard Mechanics (FEA, Plane Stress)	1.00	0.917
Experiment	0.949 ± 0.017	0.922 ± 0.018
% Error of Experiment (Average) Relative to FEA	−5.0%	+0.55%

The last step in the parametrization and construction of the cellular solid was to establish the relationships between the cell morphology, reciprocal lattice vector, and homogenized properties. The morphology of a cell can be changed by rotating the reciprocal vectors, Thus, the reciprocal vectors were rotated based on the orientation (θ) of the unit cell, $\mathbf{G}(\theta) = \mathbf{Q}(\theta)\mathbf{G}$, where $\mathbf{Q}$ is the rotation matrix. As a result, the homogenized elasticity tensor also is related to the orientation through the transformation matrix ($\mathbf{C}^{\mathrm{H}}(\theta,\rho) = \mathbf{T}(\theta)\mathbf{C}^{\mathrm{H}}(\rho)\mathbf{T}^{\mathrm{T}}(\theta)$), where $\mathbf{T}$ is the transformation matrix. In the next section, we discuss obtaining the orientation that updates the reciprocal vectors toward the optimized morphology and the material distribution that corresponds to the optimized topology.

3. Homogenization-based topology optimization

For maximum stiffness or, alternatively, minimum compliance, the homogenization-based topology optimization for the problem of multiple load cases is formulated in Eq. (5), where l and nl are the load case number and number of load cases, respectively; $\boldsymbol{F}$, $\boldsymbol{U}$, and $\boldsymbol{K}$ represent the load vector, displacement vector, and stiffness matrix, respectively; and V_g is the volume constraint. The design variables are the cell parameters (h_n) and the orientation.

$$\begin{aligned}
&\min_{\mathbf{h_n}\ and\ \boldsymbol{\theta}} \sum_{l=1}^{nl} \mathbf{F}^{\mathrm{l}}.\mathbf{U}^{\mathrm{l}} \\
&\text{s.t. :}\ \ \mathbf{K}(\boldsymbol{\rho}(\mathbf{h}_{\mathrm{n}})\boldsymbol{\theta})\mathbf{U}^{\mathrm{l}} = \mathbf{F}^{\mathrm{l}} \\
&\int_{\Omega} \boldsymbol{\rho}(\mathbf{h}_{\mathrm{n}})\, \mathrm{d}\,\Omega \le \mathrm{V_g} \\
&\quad 0 < \mathbf{h}_{\mathrm{n}} \le 1;\ n \text{ is number of parameters} \\
&-\pi \le \boldsymbol{\theta} \le \pi
\end{aligned} \tag{5}$$

In each iteration of the optimization, the current design variables and the gradient of compliance and volume with respect to the design variables are provided to the Globally Convergent Method of Moving Asymptotes [25], and new design variables were obtained. In order to initialize the orientation vector, an isotropic cell was created for each load case, the stresses were calculated, and the eigenvectors that corresponded to the maximum principal stress from all load cases were selected for the initial orientation. In the optimization process, sudden changes of $\frac{\pi}{2}$ may occur due to the repeated global optimum orientation [26]. Motivated by the penalty function used in Groen et al.

[27], a control function (P_θ) was used to penalize the sudden changes in orientation in neighboring elements:

$$P_\theta = \sum_{k=1}^{ne}\sum_{i=1}^{N}(1-\cos^2(\theta_k-\theta_i)) \tag{6}$$

The penalty function is looped over all of the elements (ne) and connected elements (N) to the k^{th} element. Eq. (6) shows that the penalty function is zero when the difference between the orientations of neighboring elements is zero or π, and the penalty function is one when there is a $\pi/2$ difference between the orientations of neighboring elements. The penalty function is added to the optimization formulation in Eq. (5), using weights that correspond to the individual objective function:

$$\min_{\mathbf{h_n}\text{ and }\boldsymbol{\theta}} w_c \sum_{l=1}^{nl}\mathbf{F}^l.\mathbf{U}^l + w_\theta P_\theta$$

$$\text{s.t. : } \mathbf{K}\boldsymbol{\rho}(\mathbf{h}_n,\boldsymbol{\theta})\mathbf{U}^l = \mathbf{F}^l$$

$$\int_\Omega \boldsymbol{\rho}(\mathbf{h}_n)\, d\,\Omega \le V_g$$

$0 \le \mathbf{h}_n \le 1$; n is number of parameters

$$-\pi \le \boldsymbol{\theta} \le \pi \tag{7}$$

where the weights are $w_c = 1/c^0$ and $w_\theta = 1/2P_\theta^0$, and c^0 and P_θ^0 are the compliance and penalty functions in the first iteration.

A $120 \times 72 \times 10\ mm^3$ bridge with one simply supported constraint and one roller constraint was selected as a test case (Fig. 8). The finite element model for the optimization consisted of linear square elements. The volume fraction constraint in this problem was 25%. The material properties that were used were Young's modulus and Poisson's ratio of $E = 950$MPa and $\nu = 0.30$. The cases of the first and second loads consisted of 1 kN applied at a distance of 40% from the left and right edges of the domain and distributed over 5% of the total length of the base of the structure. The structure was optimized using the homogenized properties obtained for three types of lattices, i.e., (a) a square cell with a rectangular hole and the use of two parameters (h_1 and h_2) to update the geometry of the lattice; (b) a Cairo pentagonal lattice with a single parameter, h; and (c) a triangular lattice with two parameters (h_1 and h_2). The optimized orientation, distribution of material, and compliance (c) utilizing the three lattices for multiple load cases (with f_1 and f_2 applied separately) and single load case (f_1 and f_2 are applied simultaneously) are shown in Fig. 9 and Fig. 10, respectively. For both test cases, it is evident that there is a distinct variation in the optimized distribution of material, but the differences between the optimized orientations for various lattices are subtle. Compared to the other lattices, the square with the rectangular hole had the highest orthotropic properties for the intermediate densities (Fig. 2), and they can be orientated with respect to the direction of the optimized principle stress. Thus, a large domain of gray areas is produced when the structure is optimized for a single load case, as observed in Fig. 10 (a). However, when the structure was subjected to multiple load cases, the optimized orientation of the local cell may not be associated with a single load in some regions of the domain, and the two directions from two load cases are not necessarily perpendicular. Therefore, to compensate, the cell becomes entirely solid in this region. Fig. 9 (a) shows that the cells in the middle region become solid to transfer the shear stresses produced by both load cases. The triangular lattice has anisotropic properties, and it provides higher stiffness in two directions with a difference of $\pi/3$ (Fig. 2 (b)). This unique characteristic of the properties of the triangular lattice was exploited in the multiple load case to provide a gray area in the middle region (Fig. 9 (b)). However, for the case of a single load, the horizontal member of the triangular lattice was oriented toward the largest principle stress to support the load (Fig. 10 (b)). Concerning the Cairo pentagonal lattice, while it has orthotropic properties for thin member thickness, it diminishes immediately when the thickness increases (Fig. 2 (c)). Thus, for both multiple load cases (Fig. 9 (c)) and single load case (Fig. 10 (c)), the lattice does not provide any advantages in the left and right regions, and the cells become solid. For the single load case, the homogenization-based design converges to solid-void, due to isotropic material properties for higher densities. However, the lattice provides a higher shear stiffness in the middle region of multiple load cases, where no perpendicular optimized direction exists, and, as a result, a semi-gray area was observed in this region (Fig. 9 (c)).

As mentioned earlier, the optimized solutions of the homogenization-based topology are based on infinite periodicity with no requirement for the connectivity of the adjacent lattice. Disconnected lattices are not consequential with an infinite number of cells, but they become an issue when the lattices are transformed to finite sizes. In the next section, the construction of a coherent, shape-preserving orientation to establish interconnected finite size lattices is discussed.

4. Projection of cellular solids using Fourier series

After determining the optimized orientation (θ^*) in the previous section, the reciprocal lattice vectors were updated, i.e., ($\boldsymbol{G}(\theta^*) = \boldsymbol{Q}(\theta^*)\boldsymbol{G}$). It has been shown that when $\boldsymbol{G}$ is a function of $\theta(\vec{\boldsymbol{r}})$, the result of adding the Fourier series fails to reproduce the desired lattices [20]. Rumpf and Pazos [20] suggested using a mapping function, Φ_{pq}, which accumulates the phase along the direction of the reciprocal lattice vectors. Therefore, the reciprocal lattice vector, rotated according to the optimized orientation ($\boldsymbol{G}(\theta^*)$), is decomposed to rotational and irrotational components in order to reconstruct the orientation and size of the cells. Decomposition of a vector field to rotational and irrotational terms provides significant insights in various applications in fluid mechanics [28] and solid mechanics [29,30]. In the current application, a mapping function was created from an irrotational component of a reciprocal lattice vector to project the lattices from a homogenized space to a finite-sized cellular solid. In general, the reciprocal lattice vectors are not solely rotational or irrotational, and they contain characteristics of both the orientation and the spatial period. Analogous to the Helmholtz-Hodge representation of vector fields [31], reciprocal lattice vectors in a domain D are decomposed to irrotational and rotational components, and the mapping function related to the irrotational component is constructed as follows:

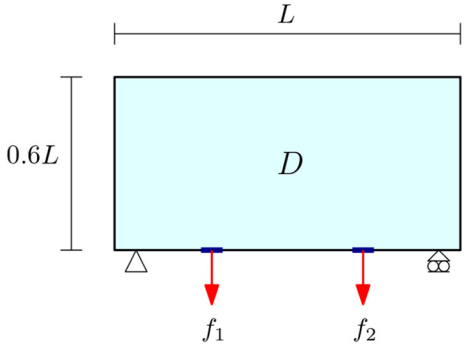

Fig. 8. Bridge test case subjected to multiple load cases

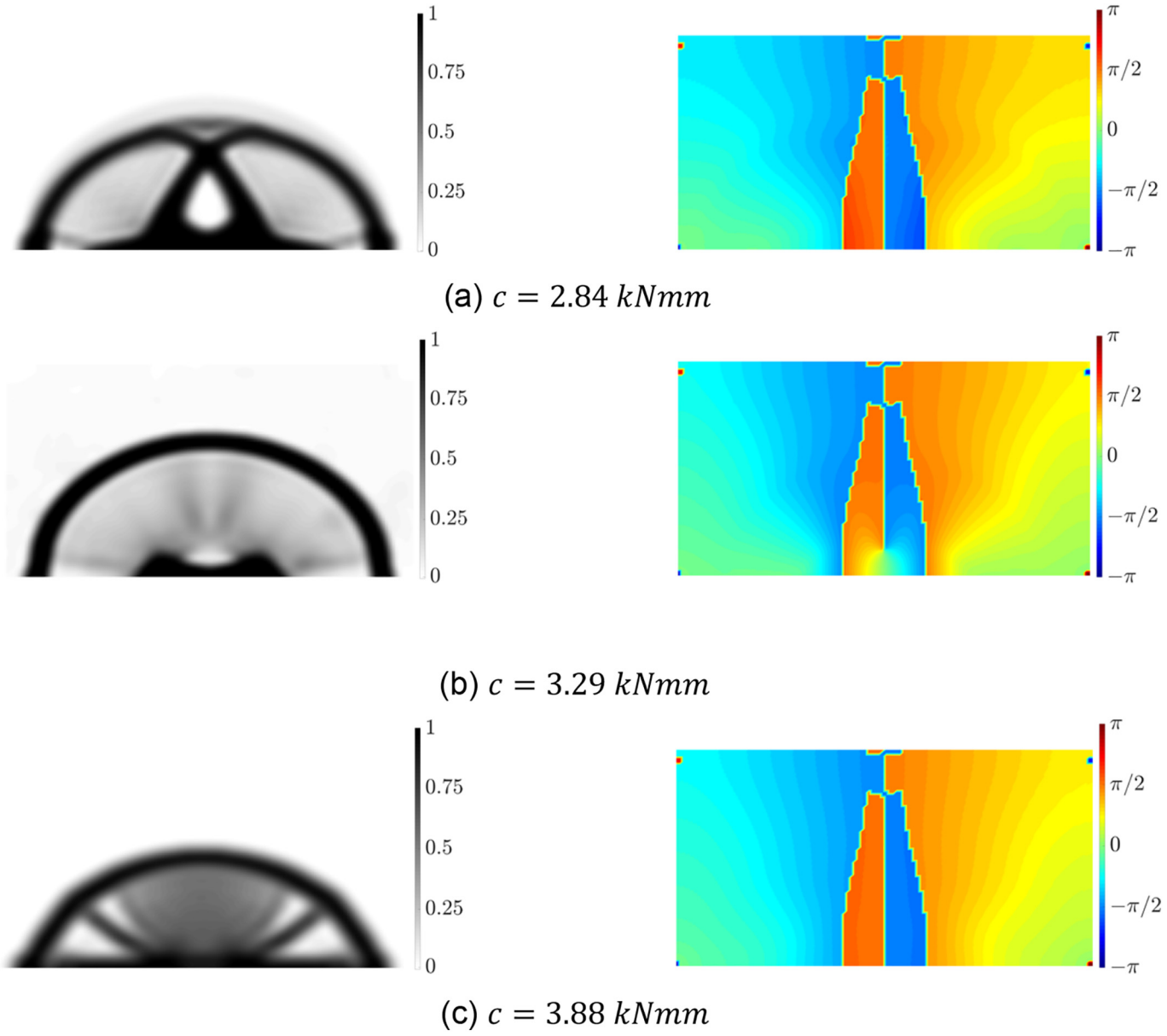

Fig. 9. Multiple load cases optimized material distribution and orientation for: (a) a square cell with a rectangular hole; (b) a triangular lattice; (c) a Cairo pentagonal lattice

$$\nabla^2\Phi^n_{pq}(xy) = \nabla\cdot\frac{G^n_{pq}(\theta)}{\Lambda} \text{ on D}$$

$$\frac{\partial\Phi^n_{pq}}{\partial\Gamma} = G^n_{pq}(\theta)\cdot\eta \text{ on } \partial\Gamma \tag{8}$$

where $\partial\Gamma$ is the boundary of the domain, and $\boldsymbol{\eta}$ is normal to the boundary. The field lines of the irrotational component of a reciprocal vector are the level sets of Φ^n_{pq}. To ensure the uniqueness of the irrotational function, the following condition was enforced: $\nabla\Phi^n_{pq} \times \boldsymbol{G}^n_{pq} = 0$.

While solving Eq. (8) with the above constraint extracts the irrotational component, the Fourier series representation based on Φ_{pq} becomes distorted due to the irregularities of the reciprocal lattice vector. The source of these irregularities is either differences of π in the orientation of periodicity (as shown in the optimized orientations in Fig. 9 and Fig. 10), or the singularities (or degenerate points) occuring due to the presence of the repeated global minima. To capture the irregularities and create a locally continuous vector field, a shape-preserving interpolation concept was used that decoupled the shape and direction [32,33]. The first step was to capture the inconsistency of the propagation and the degenerate points by screening the vector field in the local triangular or tetrahedral elements in the structural domain. A vector field is generated from the optimized orientation ($\mathbf{v} = [cos(\theta^*), sin(\theta^*)]$). The dot product of the vectors of the two vertices (V_i) identifies the irregularities in the local element; if the product of all dot products between pairs of vectors is not positive, then the element contains degenerate points (Fig. 11. (a)); otherwise, if some dot products are negative, there is a π difference in orientation (Fig. 11. (b)). For the elements with a degenerate point (point D in Fig. 11. (b)), a vertex at the degenerate point with $\mathbf{v} = 0$ (due to the inability to determine the orientation [33]) is inserted to construct sub-elements without an inner degenerate point. Then, an interpolation is generated for each element ($\boldsymbol{v}_{en}$) to reconstruct the unit vector field that is consistent with the flow of cell propagation in the neighboring cells:

$$v_{en} = \zeta_1 v_1 + \sum_{i=2}^{nv}\zeta_i V_i v_i \tag{9}$$

where nv and ζ are number of element vertices and element shape functions.

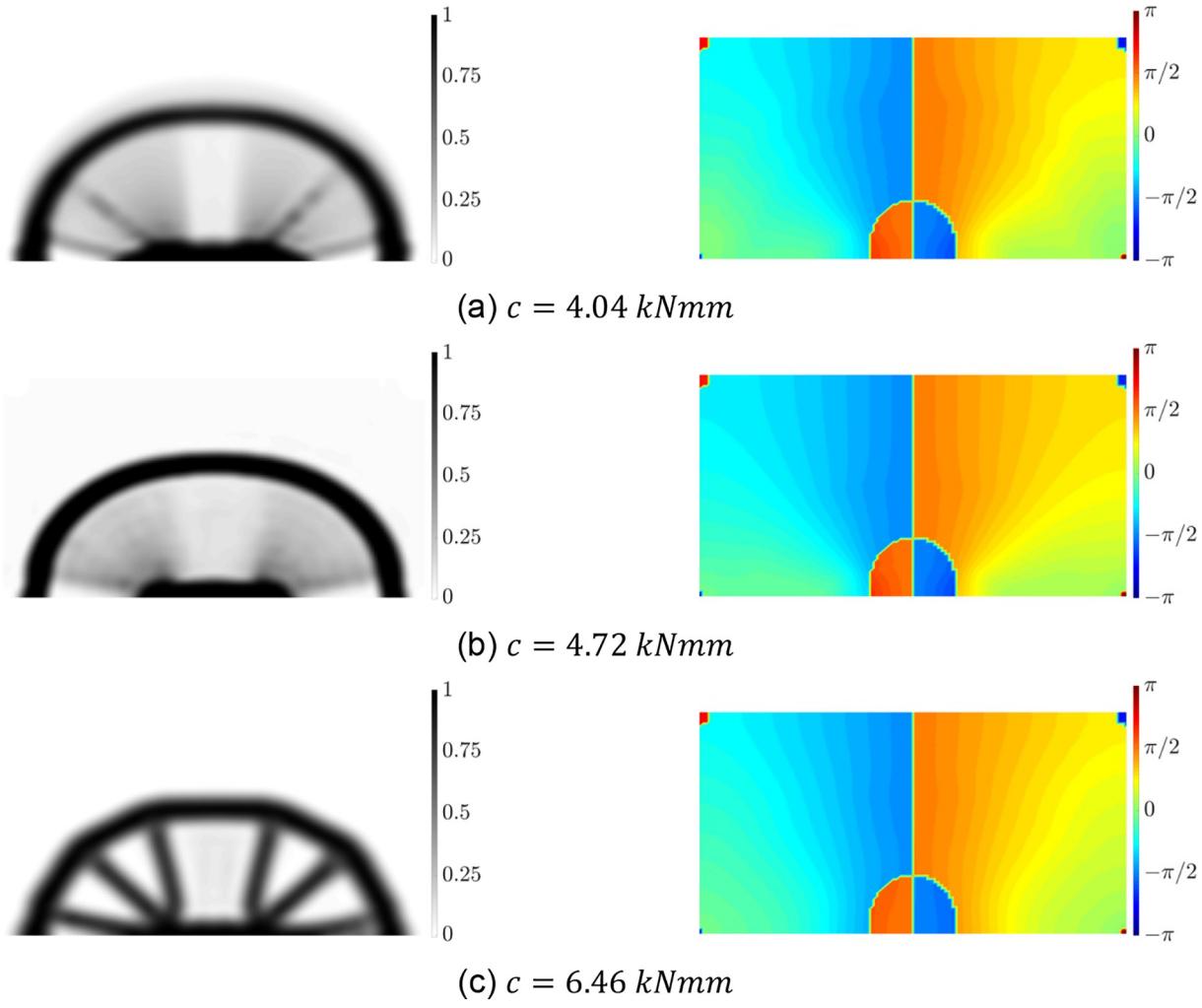

Fig. 10. Single load case optimized material distribution and orientation for: (a) square cell with a rectangular hole; (b) triangular lattice; (c) Cairo pentagonal lattice

The above procedure creates a coherent orientation to rotate the reciprocal lattice vectors, but the original geometry of the cell may not be preserved in the projection, i.e., the cell is compressed or stretched. To this end, Groen and Sigmund [17] suggested finding the average lattice spacing by using the gradient of the mapping function and adjusting the period of the lattice accordingly. Allaire, Geoffroy-Donders, & Pantz [18] suggested obtaining a local dilatation factor (γ) and multiplying the vector field by e^{γ}. This method was used in the current work. Therefore, the reciprocal lattice vector is multiplied by e^{γ}, i.e., $\boldsymbol{G}_{pq} = e^{\gamma}\boldsymbol{G}_{pq}$, where γ depends solely on the optimized orientation (θ^*):

$$\nabla\gamma = (-\nabla \times \mathbf{v})\mathbf{v} + (\nabla \times \mathbf{v})\mathbf{v} \tag{10}$$

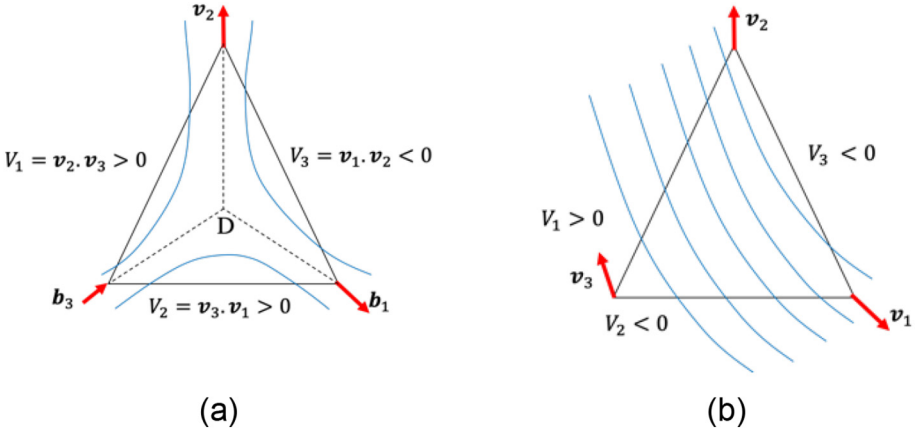

Fig. 11. (a) Existence of the degenerate point; (b) Inconsistency in the propagation of the flow of cells

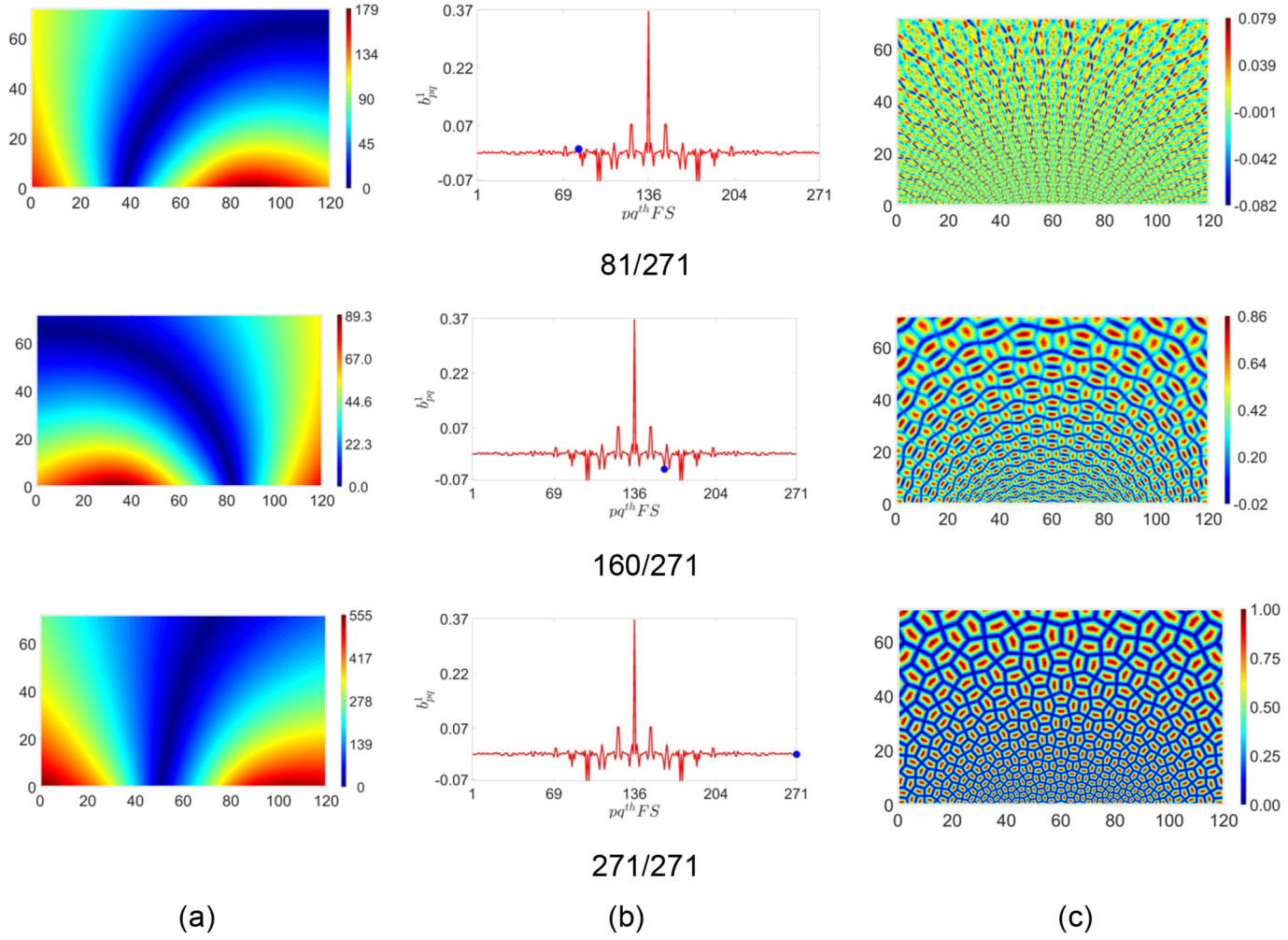

Fig. 12. Projection method using Fourier series for Cairo pentagonal lattice: (a) mapping function (Φ); (b) amplitude; (c) analog lattice (ψ) created up to 81, 160, and 271 terms

and **v** is perpendicular vector to **v.** In addition, we modified the periodicity, Λ, using a coefficient ($\not\angle\Lambda$) to enforce approximately the same cell area for the three lattices so that there was a level of consistency when comparing the performance as well as enforcing the minimum feature size for the different types of lattices in the next sections. The area of square cell with the

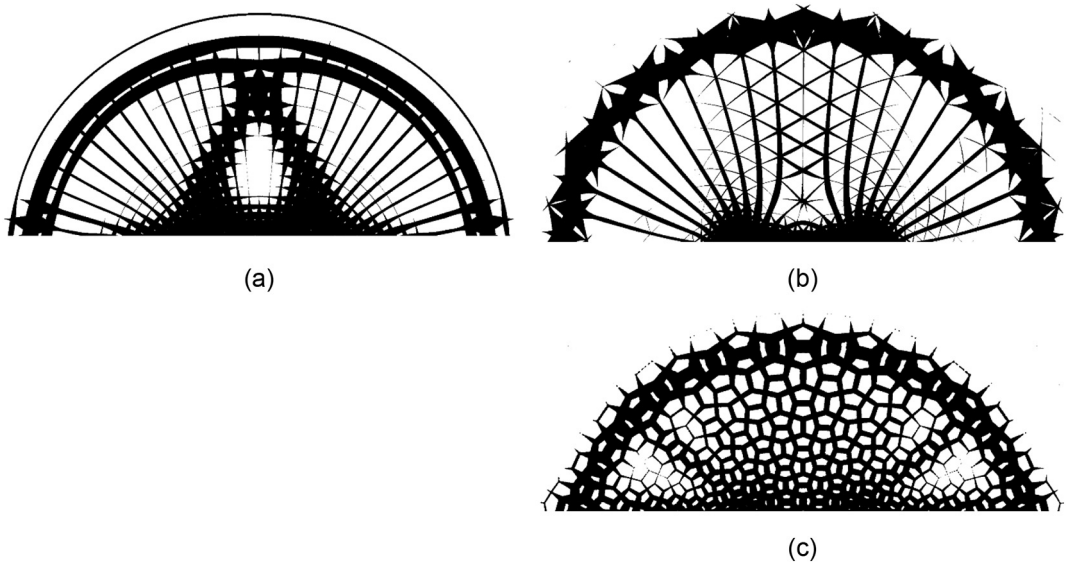

Fig. 13. Multiple load cases binary lattices (Ω_1) for: (a) square cell with a rectangular hole; (b) triangular lattice; (c) Cairo pentagonal lattice

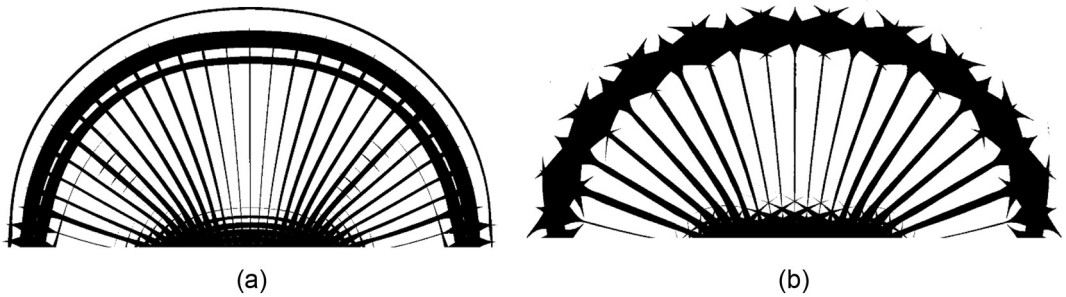

Fig. 14. Single load case binary lattices (Ω_1) for: (a) square cell with a rectangular hole; (b) triangular lattice

rectangular hole was considered as the reference, thus $\ell = 1, \sqrt{4/\sqrt{3}}$, and $\sqrt{8}$ for squares with a rectangular hole, triangular, and Cairo pentagonal lattices, respectively.

The last step in the projection procedure is to create an analog lattice by using the mapping function that corresponds to each reciprocal lattice vector (Eq. (11)). Then, an analog lattice is thresholded with the optimized material distribution (ρ^*) obtained from the homogenization-based topology optimization to find the binary cellular structures (Eq. (12)). When there is more than one parameter that describes the initial geometry of the cell, the final projected shape is obtained through the union of the binary lattices (Eq. (13)).

$$\psi_n = \mathrm{Re}\left\{\sum_{pq} b_{pq}^n \exp\left(j\phi_{pq}^n(r)\right)\right\} \tag{11}$$

$$S_n = \left(\psi_n \le h_n^*\right) \tag{12}$$

$$\Omega = \mathrm{US}_n \tag{13}$$

$\Lambda = 5$ was selected for the results shown in this section and in Section 5. Fig. 12 shows the phase (or mapping function (Φ)), and the amplitude of the term numbers 81, 160, and 271 in the Fourier series and the analog lattice created up to these terms. As can be seen, the final analog lattice created by summing the 271 terms fully obtains the Cairo pentagonal cellular solid. For the projection step, a finer structured triangular mesh with 15 elements per unit length was used in order to capture the small features. The binary lattices (Ω_1) for multiple load cases and a single load case are shown in Fig. 13 and Fig. 14. The reported binary lattices may include floating members (because of the size of the mesh), and members and holes that have small sizes that cannot be fabricated due to the minimum feature size in the manufacturing process. In the next section, the manufacturability characteristics of reconstructed cellular solids are investigated, and a post-processing method is developed to ensure the feasibility of additively manufacturing the cellular solids.

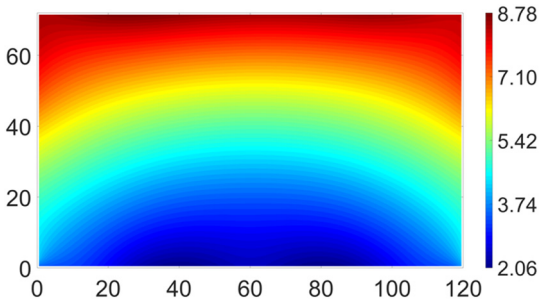

Fig. 15. Feature sizes for the Cairo pentagonal cellular solid

5. Post-processing of the projected, spatially-varying cellular solids

Two post-treatments for the projected square cell with a rectangular hole have been suggested in the literature. The first treatment consists of two parts, i.e. 1) utilizing a smoothed Heaviside projection to keep only the members above a certain thickness [17]. Since an explicit thickness is not enforced in this method, the projected feature size based on local periodicity is obtained in the second step, and the lattices are modified based on the allowable thickness. Then, the free-hanging members are removed based on an iterative finite element analysis and the identification of members that have low strain energy. 2) Explicitly enforcing the minimum feature size [18]. In the second step, the closed holes are filled and the complement of the filled region is obtained to identify and remove the free-hanging members. In the current research, method 2 was modified based on our experience with projected design performance, and it was extended to be applicable to various types of lattices. Based on the modified periodicity introduced in the previous section ($\ell\Lambda e^{-\gamma}$), post-processing consisting of three steps was developed for the periodic microstructures using n number of characterizing parameters. These steps are explained based on the assumption that the characterizing parameters (h_n) are related to the solid members in the cell.

5.1. Modification based on the minimum periodicity of the features and the thickness of the lattice

First, the smallest feature periodicity (t_f) within a unit cell in Cartesian coordinates was identified. The minimum periodicity of a triangular lattice in Cartesian coordinates is $\sqrt{3}\Lambda/2$ (see Fig. 5). The Cairo lattice includes 8 complete pentagons, so the minimum periodicity is $\Lambda/\sqrt{8}$. To determine the minimum size of the features for each lattice, the modified periodicity ($\ell\Lambda e^{-\gamma}$) is multiplied by 1, $\sqrt{3}/2$ and $1/\sqrt{8}$ for a square with a rectangular hole, triangular, and pentagonal lattices, respectively. Fig. 15 shows the distribution of the feature sizes for the Cairo pentagonal cellular solid. Then, the design domain, D, is divided to two subsets according to the periodicity of the features. The first subset, D_1, is defined by the cells that have feature sizes smaller than two manufacturable thicknesses ($t_f < 2h_{min}$). The reason for choosing $2h_{min}$ was that both holes and solids with the minimum feature size of h_{min} cannot coexist with a periodicity lower than $2h_{min}$. The h_{min} in this research was 0.8

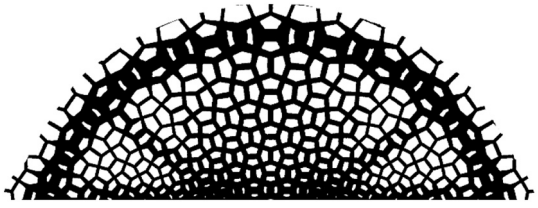

Fig. 16. Projected shape, Ω_2, after increasing the thicknesses of the members in the regions where $\rho^* > \rho_{th}$

mm. Then, a single-step thresholding function is applied to each parameter h_n, and $\widetilde{h}_n$ is created. The step function forces $\widetilde{h}_n$ to be one and zero for regions with $\rho^* \geq 0.5$ and $\rho^* < 0.5$, respectively.

The second subset is defined by all the points in domain D, where $t_f > 2h_{min}$. One suggestion (hereinafter referred to as Method-A) is to modify the thickness of the member ($t_f h_n$) in the lattice using the following conditions, i.e., (a) if $t_f h_n < h_{min}/2$, then $\widetilde{h}_n = 0$ to remove members with very small thicknesses and (b) if $h_{min}/2 \leq t_f h_n < h_{min}$, then $\widetilde{h}_n = h_{min}$, to bring the members with moderately small thicknesses to the minimum thickness [18]. However, our experience has indicated that removing individual members in a cell based on minimum thickness compromises the structural performance. As is shown later in Section 5, the process results in long and thin members in the middle area of the structures. These unsupported members with high aspect ratios bend under applied loads, thereby degrading the stiffness-to-weight ratio of the overall structure. Thus, we suggest another method (hereinafter referred to as Method-B), which consists of applying the following conditions for the lattices in the second subset, i.e., (a) if $\rho^* > \rho_{th}$ (in this case $\rho_{th} = 0.1$) and $t_f h_n < h_{min}$, then $t_f \widetilde{h}_n = h_{min}$, and (b) if $\rho^* < \rho_{th}$, then $\widetilde{h}_n = 0$. Fig. 16 shows the projected shape, Ω_2, after applying this condition. By comparing the projected shapes in Fig. 16 and Fig. 13 (c), it can be seen that the thicknesses of the members located in the lower right and left domains are increased.

5.2. Filling cells with small holes

Data manipulation procedures, such as those presented in Section 5.1, use point-based functions, such as the local periodicity, but this approach has the disadvantage of not being able to fully fill the small voids in the projected cells, which has adverse effects on the manufacturability and performance of the design. Thus, in this step, regions are implemented instead of data manipulation procedures to identify small holes in the projected cells. First, the subset D_3 is created by thresholding the analog lattice (Fig. 12 (c)) with h_{min} (Fig. 17 (a)). The regions are created from the complement of the union between D_3 and the projected shape, Ω_2 (Fig. 17 (b)). Then, the diameter of the largest inscribed circle (a measurement of porosity) is calculated for each region. The regions with inscribed circle diameters less than 1.05 h_{min} are filled (Fig. 17 (c)). By comparing the new projected shape (Ω_3) in Fig. 17 (c) and projected shape (Ω_2) in Fig. 16, it is apparent that the small holes close to the loading application and the outer border of the shape are filled.

5.3. Removal of floating members and smoothing the boundaries

The last steps in the post-treatment are 1) to remove the floating members and 2) to smooth the boundaries. First, the closed holes with areas smaller than a threshold are filled temporarily (Fig. 18 (a)). The threshold is obtained based on a fraction (e.g., 1/2) of the largest region identified in the subset D_2 and $\rho^* > \rho_{th}$. This threshold is necessary for the cases that have large holes inside the bounded structure with free-end members. The complement is taken and divided into regions (black areas in Fig. 18 (b)). The boundaries of the black regions are created, and a Delaunay triangulation is utilized for each region to create an outer polygonal shape. Then, the number of triangles in the Delaunay triangulation is reduced by a factor of 0.8 to create a slightly smoother boundary, and the vertices within the boundary are added to the region (Fig. 18 (c)). Then the complement of the complement is found, as shown in Fig. 18 (d) in which the temporarily-filled areas are emptied. This process was repeated until all of the floating members were removed. In addition, after removing the floating members, the points that are located between the boundary of the projected shape and a smoothed boundary created by a non-uniform rational basis spline (NURBS) can be added to the projected shape in order to create a uniform outer boundary. The final post-processed cellular solid, Ω, is shown in Fig. 18 (e). In order to perform a detailed, 2D finite-element analysis, Bezier splines were used to convert the post-processed results to CAD geometries. Fig. 19 shows the CAD geometries for the post-processed optimized designs with square with rectangular holes, triangular lattice, and Cairo pentagonal lattice for multiple load cases and a single load case with two periodicities, i.e., $\Lambda = 5$ and 7. A case number is assigned to each design that will be used in the next section to compare the performances of various designs.

6. Comparison of the performances of various spatially-varying cellular solids

Due to the post-processing, the final designs can have relative volumes that are different from those of the optimization constraint.

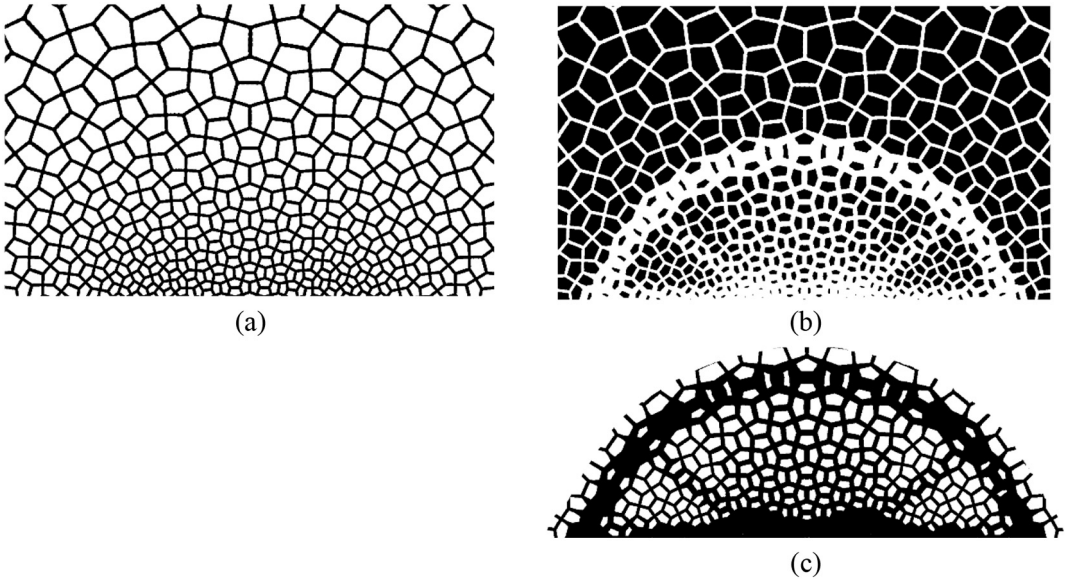

Fig. 17. (a) Analog lattice thresholded with h_{min} (subset D_3); (b) region created by the complement of the union between D_3 and the projected shape Ω_2; (c) projected shape (Ω_3) with filled small holes

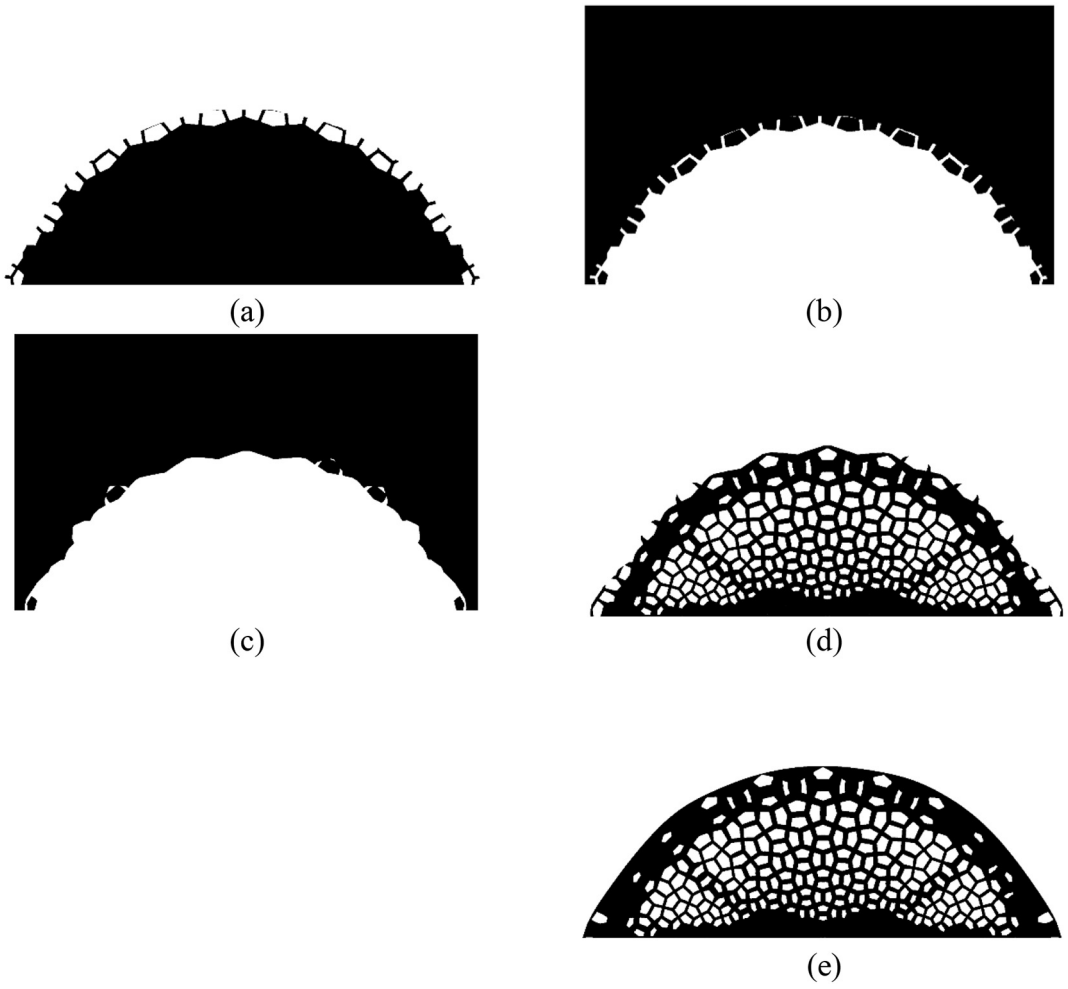

Fig. 18. (a) Temporary filling of the small closed holes; (b) Complement of (a); (c) removing the floating members; (d) projected shape after removing the floating members; (e) the final projected shape (Ω) after smoothing the boundaries

Thus, the slope of the force-displacement curve per unit surface area of the front face is used as a performance indicator to compare different designs. For a linear force-displacement relationship this is

$$\text{Specific Stiffness} = \frac{P}{\delta A} \tag{14}$$

where P is the applied load, δ is the maximum deflection, and A is the area of the front face of the structure. Loads and boundary conditions were applied to the same parts of the domain as was done in the optimizations. The properties of the material that were used were Young's modulus and Poisson's ratio of $E = 950MPa$, and $\nu = 0.30$. The surface geometries were meshed with two-dimensional linear finite elements, and linear static analyses were performed.

For the first analysis, the post-processing Method-A was used for a multiple-load cases with a triangular lattice bridge design, and one load was applied to the left side. Fig. 20 shows the projected design and vertical displacement, where A^{Ω} and A^{D} are the areas of the front face of the projected design and the baseline model, respectively. As can be seen, this post-processing method resulted in the removal of almost every small cross member, leaving the larger vertical members completely unsupported with no means of transferring the lateral load between them. Without the supporting structures, they bend easily, and the bridge is left with very low stiffness.

Post-processing Method-B was applied for the following two triangular cell bridge designs. The design of the first bridge was optimized for multiple load cases, and a single load was applied, as was the case for the design in Fig. 20. Fig. 21 shows the following: (a) with the post-processing Method-B, the small cross members were retained, which solved the issue of the bending of unsupported members, and the overall specific stiffness of the bridge was increased by 71%. The second bridge was optimized for a single load case, and two different analyses were performed. In the first analysis, a 1 *kN* load was applied to the left side (Fig. 21 (b)). Since the structure was optimized for the single load case with loads applied to both sides, it handled the unsymmetrical force less efficiently due to the large hole in the middle. A load applied to the left side cannot transfer directly across the hole to the right support, and this causes a lateral bending response; its specific stiffness was 17% lower than the bridge that was optimized for multiple load cases. In the second analysis two 1 *kN* loads were applied simultaneously (Fig. 21 (c)). The bridge performed more efficiently under the single load case for which it was optimized, i.e., the vertical deflection only increased by 1.4x despite carrying a total load that was 2x greater.

Analyses also were performed for the other eight cases mentioned in the previous section (Fig. 19). Table 2 summarizes the results for the designs with multiple load cases, and Table 3 summarizes the results for the designs with a single load case. By comparing the contents of Table 2 and Table 3, it is apparent that the specific stiffness of the homogenized design was closer to the projected design for multiple load cases than it was for the single load case. This occurred because the thicknesses of more members were increased to the manufacturable thickness in the projected shape of the design of the single load case.

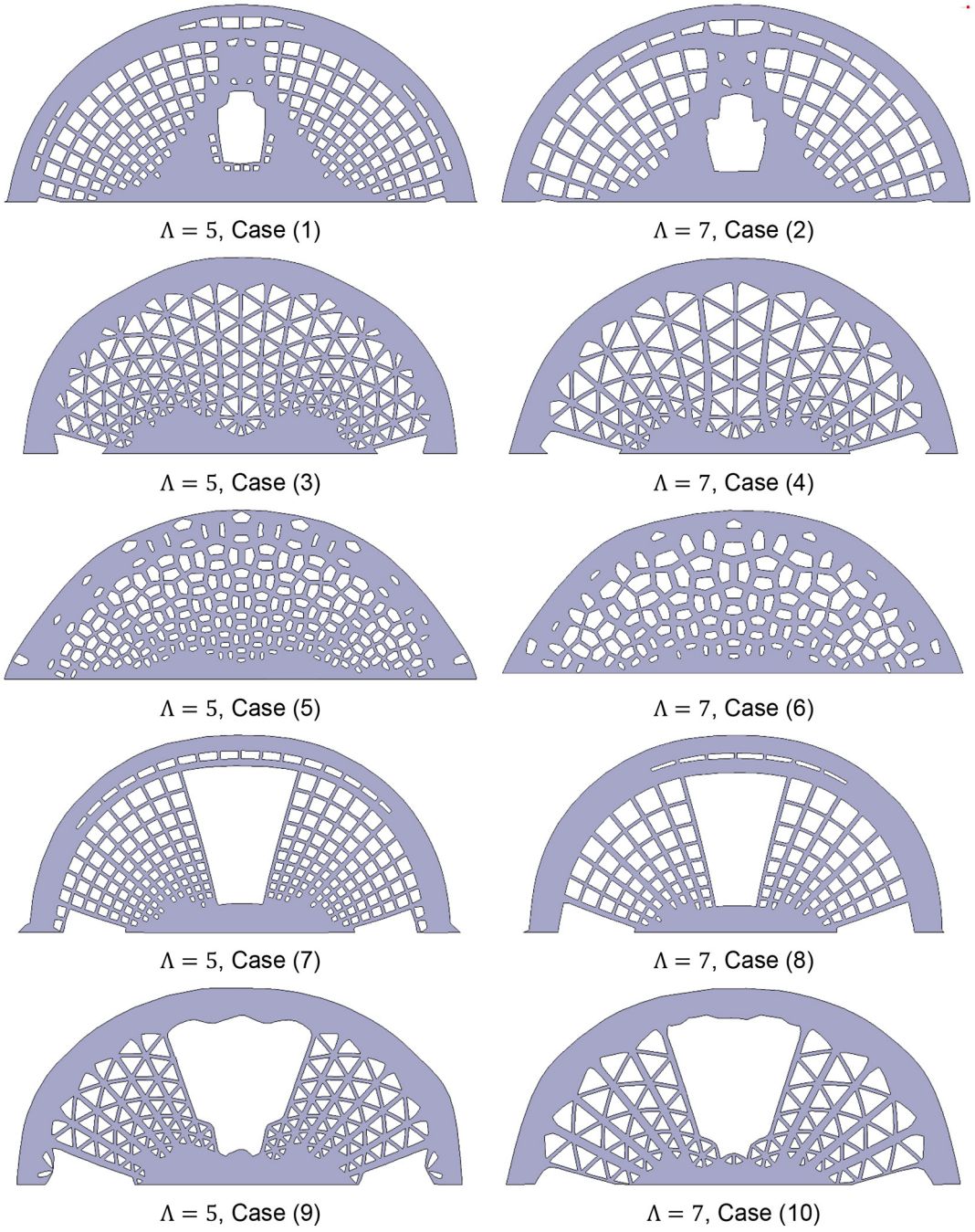

Fig. 19. CAD geometries for post-processed optimized designs subjected to multiple-load cases (Cases (1)-(6)) and single load case (Cases (7)-(10))

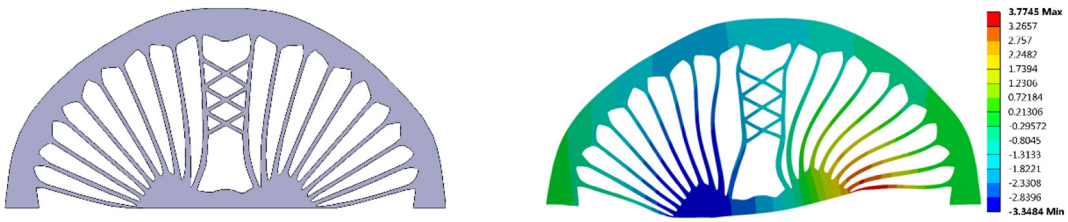

(a) $A^{\Omega}/A^{D} = 0.214$ (b) $c = 6.68\ kNmm$

Fig. 20. Bridge optimized for multiple load cases using post-processing Method-A: (a) CAD geometry; (b) true scale vertical deformation plot [mm]

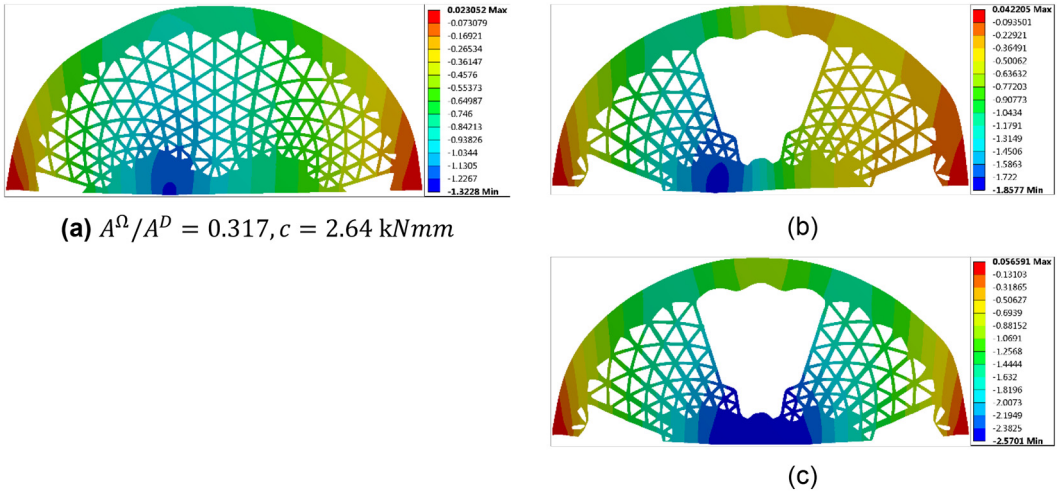

Fig. 21. Optimized bridge designs with true scale deformation plots [mm]: (a) Multiple load case design with one load applied; (b) single load case design with one load applied; (c) single load case design with two loads applied

For the square lattice structures, while the smaller periodicity led to a better structural performance (case (1) compared to case (2) in Table 2), the smaller periodicity also results in smaller cells, some of which are filled in order to satisfy the minimum manufacturing feature size. As a result, both periodicities result in similar specific stiffnesses. The performance of case (2) was the best of all of the designs. The triangular lattice with the smaller periodicity (case (3) in Table 2) had the most frontal surface area. The large increase in material over the value of the optimization target was due to the post-processing manufacturing constraint filling in small holes where the cell orientations converge to the points of load application. Large solid regions were apparent around these areas in Fig. 19, Case (3). By comparing Case (4) to Case (3), it is clear that the larger periodicity of Case (4) resulted in fewer features that were smaller than the manufacturing constraint, and accordingly its area was 11% less than that of case (3). The deflection was increased by a roughly-equal proportion of 11%, so the overall specific stiffness was similar for both periodicities. The Cairo lattice structures (cases (5) and (6) in Table 2) had the lowest specific stiffnesses of the multiple-load cases designs. Case (5) had a smaller periodicity, and it showed a slight increase in specific stiffness compared to Case (6).

Table 2
Performance Comparison of Multiple Load Case Bridge Designs

Case	A^{Ω}/A^{D}	Compliance ($kNmm$)	Specific stiffness (N/mm^3)	
			Projected design	Homogenized design
(1)	0.272	2.94	0.289	0.320
(2)	0.250	3.18	0.290	
(3)	0.317	2.64	0.277	0.281
(4)	0.282	2.94	0.279	
(5)	0.269	3.62	0.237	0.238
(6)	0.264	3.74	0.234	

Table 3
Performance Comparison of Single Load Case Bridge Designs

Case	A^{Ω}/A^{D}	Compliance ($kNmm$)	Specific stiffness (N/mm^3)	
			Projected design	Homogenized design
(7)	0.264	4.86	0.361	0.458
(8)	0.294	4.16	0.383	
(9)	0.273	5.14	0.329	0.392
(10)	0.260	5.08	0.350	

For the results of the single load case design, which are summarized in Table 3, the specific stiffness was higher for larger periodicities with two loads applied simultaneously. For the single load case, there was only one principal stress direction field. If the alignments of the walls of the cells in this direction field were perfect, the square and triangular lattice structures would have maximum stiffness irrespective of the number of cells. Therefore, decreasing the periodicity in the optimized structures has a lessened effect on stiffness, while more material still can be added to satisfy the manufacturing constraint.

Another interesting observation that can be made from comparing Table 2 and Table 3 is that, even though the square lattice structures in the design of multiple load cases have approximately 4% higher specific stiffness than triangular lattices, this is increased to 9.5% for the single load case. This shows that, while filling the small holes due to the manufacturing constraint decreased the specific stiffness of the triangular lattice design, it still provides acceptable performance because of its ability to transfer shear in the middle region for the multiple load cases.

In summary, three main conclusions can be extracted from these analyses:

1. Reducing periodicity will increase structural performance up to a point at which limitations in manufacturing precision outweigh increases in stiffness. Future advances in additive manufacturing techniques to fabricate microstructures with smaller feature size will allow for smaller cells and additional gains in performance, but, ultimately, there will be diminishing returns.

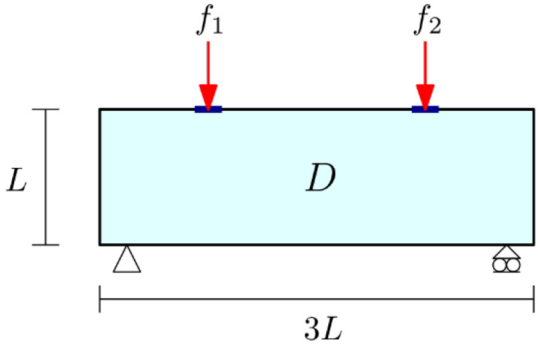

Fig. 22. Three point-bending test case subjected to multiple load cases

Table 4
Linear Specific Stiffness of Three-Point Bending Designs

Case	Geometry	Area (mm^2)	Maximum Deflection (mm)		Specific Stiffness (N/mm^3)		
			FEA	Experiment	FEA	Experiment	% Error
(11)		4447	0.760	0.774	0.296	0.291	-1.7%
(12)	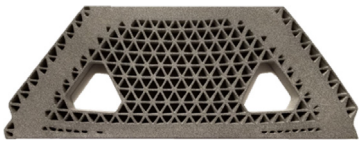	5161	0.606	0.647	0.320	0.300	-6.3%
(13)	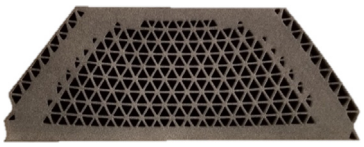	5343	0.556	0.575	0.336	0.326	-3.0%

2. For the designs of single load case in which the walls of the cells are aligned with the load paths, the point at which manufacturing limitations outweigh increases in stiffness will occur sooner. (See Table 3.)
3. The orthotropic square lattice cell can provide the most efficient use of material for the single load case, but since the stiffness is only high in very specific directions, the structures may have lower performance in multiple load cases where shear stresses exist in some regions.
4. The triangular lattice cell produces macrostructures that are capable of transferring shear, so it may be better to use them in situations where there are larger numbers of load cases.

7. Experimental evaluation of additively-manufactured, spatially-varying cellular solids and SIMP designs

Experimental testing was performed on three-point bending structure designs obtained using conventional SIMP topology optimization and the method described in this paper with triangular lattices. Each structure was generated with a rectangular design space that had a 3:1 aspect ratio. The height of the design space (L) was 62 mm with an out-of-plane thickness of 15 mm (Fig. 22). The optimized results were obtained using a Young's modulus and Poisson's ratio of $E = 950MPa$ and $\nu = 0.30$ for multiple load cases with loads of $1kN$. An optimized design was obtained using the SIMP method with 186×62 elements (Table 4, case (11)). The same number of elements was used to determine the homogenization-based topology optimization designs. Then, the optimized homogenized material distribution was projected using $\Lambda = 4.4$ and 15 elements per unit length (Table 4, case (12)). The holes in the lower left and right sides of the case (12) domain were filled with triangular lattices, and the periodicity was changed slightly ($\Lambda = 4.5$) to also fill the bottom edge (Table 4, case (13)). The results in Table 4 show that the specific stiffness of the triangular lattice design (case (12)) outperformed SIMP by 8% for a load applied to the left side. Filling in the large holes with lattices in case (13) increased the performance by 13% over the SIMP design.

Along with the computational analysis, the three designs were additively manufactured by Multi Jet Fusion with PA 12 material. The printed specimens were painted, stamped with a speckle pattern, and they were tested experimentally using Digital Image Correlation (DIC) in a three-point bend fixture with the left offset load. The experimental results were compared with the computational results in Table 4. Fig. 23 (a) shows the applied force (per unit area of the front faces of the structures) versus the displacement of the testing machine's crosshead. Fig. 23 (b)-(f) show the spatial distributions of the vertical component of displacement captured by DIC at the events marked in Fig. 23 (a), which can have minor discrepancies compared to the crosshead displacements because the DIC was not able to track the point of load application at the extreme edges of the structures.

The linear parts of the experimental curves agreed well with the linear computational analysis. Case (12) had a 3% higher specific stiffness (slope of the curve) than the SIMP design, while the lattice design of case (13) had a slope that was 12% higher than case (11).

Interestingly, at large displacements in the nonlinear range the lattice designs showed a major strength advantage over the SIMP structure. The SIMP design lost stiffness early when its comparatively few and large structural members deformed significantly and lost their ability to efficiently transfer load to the supports. It reached a maximum load of 4.37 kN before it failed catastrophically at a crosshead displacement of 8.9 mm (Fig. 23 (b)).

The triangular lattice design of case (12) continued to carry larger loads well beyond the strength of the SIMP design, reaching a maximum of 7.93 kN. Its many small, closely-spaced lattice members provided redundant load paths that the SIMP design did not have, and this allowed it to achieve much higher deflections and forces by redistributing the internal loads as the individual small members reached their limits. An easily observable example of this load path redundancy is evident in point (c) of the load-displacement curve, where a single small strut fracture occurred (Fig. 23 (c)) but the overall structure continued to carry increasing loads. After the strut fracture, a different region of the lattice material buckled at 9.5 mm of crosshead displacement, but the internal loads were redistributed again, and the design continued to deform until 10.2 mm (point (d) and Fig. 23 (d)) before failing completely.

The triangular lattice design of case (13) similarly experienced much higher strength than the SIMP equivalent, and it also had a similar progressive failure. Fig. 23 (e) shows the structure at 8 mm of crosshead displacement after an initial local buckling event. Subsequently, it continued to deform while carrying a load per unit area 35% larger than the maximum of the SIMP design. Two small members fractured at 9.2 mm of crosshead displacement (Fig. 23 (f)), and complete failure occurred subsequently at 9.9 mm.

The results of these experiments led us to conclude that the method described in this paper can produce designs with higher linear stiffness than conventional SIMP topology optimization. In addition, as a side effect of the use of cellular solids, the strength per unit area was shown to be as much as 57% greater than SIMP at large displacements due to the robust nature and progressive failure behavior of the triangular lattices.

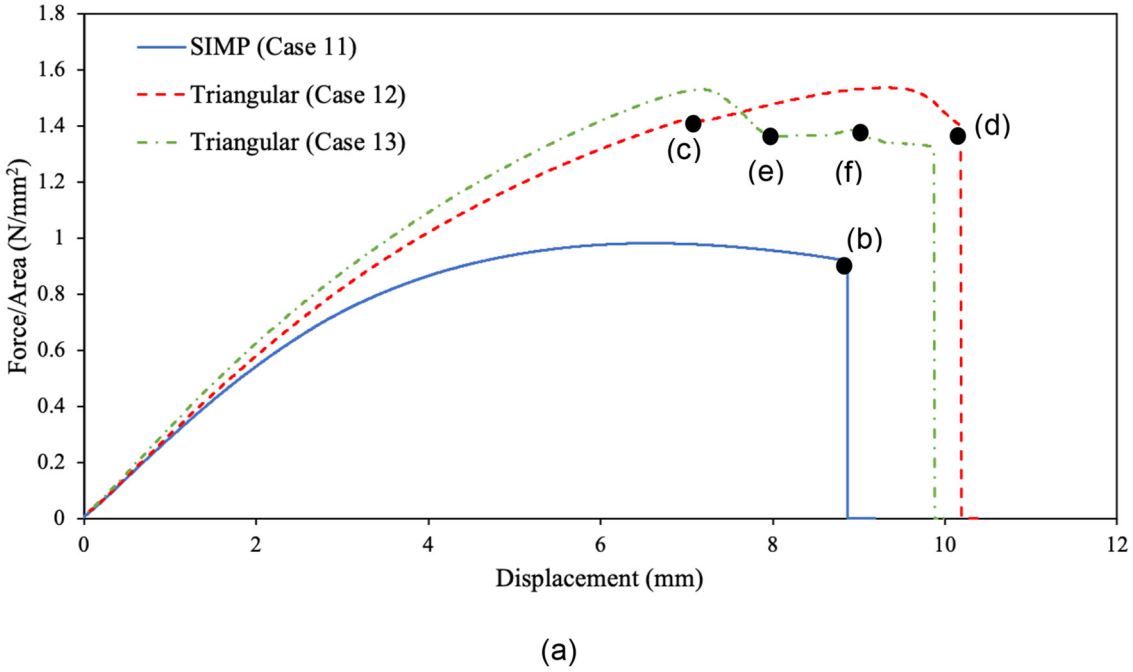

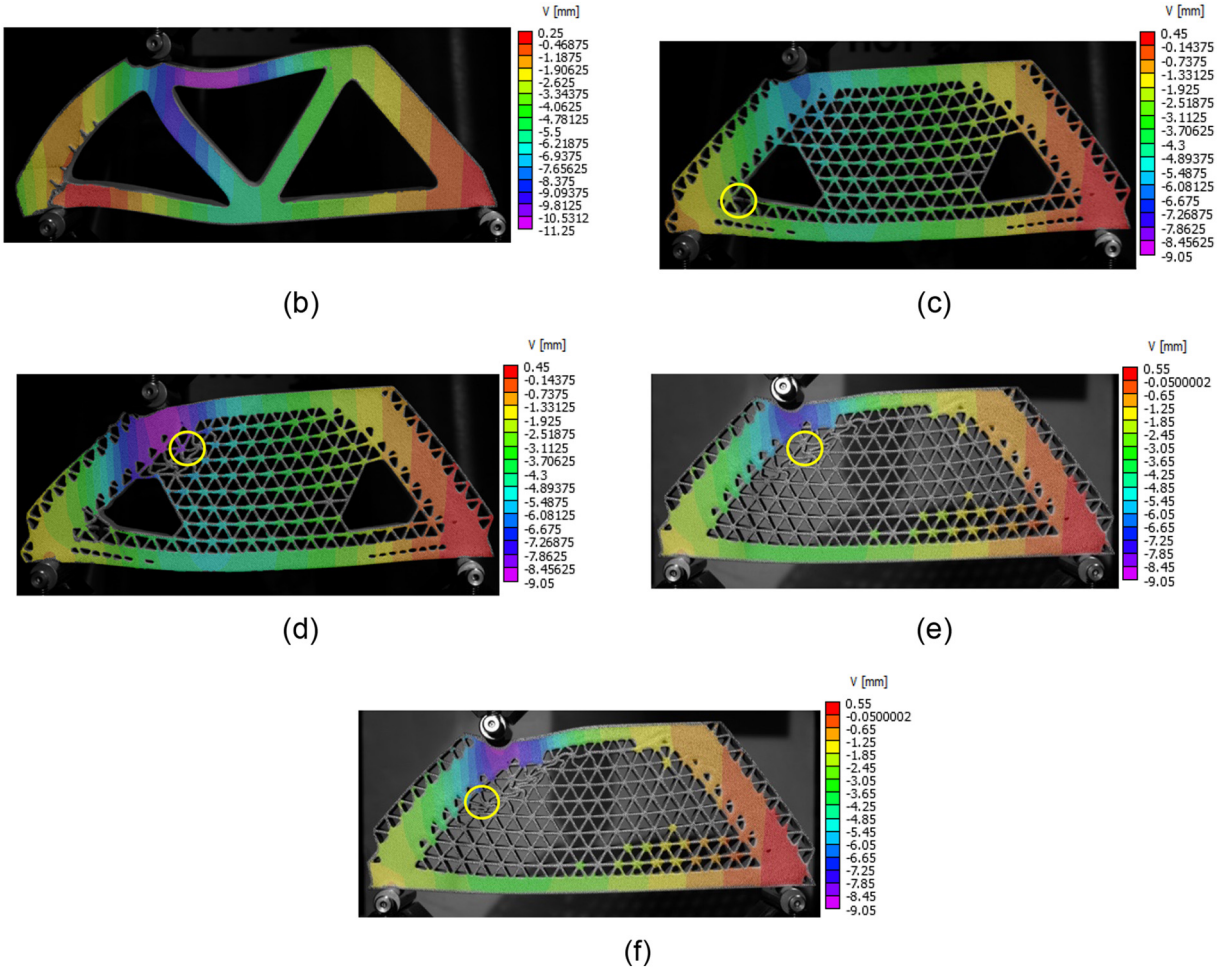

Fig. 23. Three-point bending tests: (a) Force per unit frontal surface area versus crosshead displacement at the point of load application; (b) the SIMP specimen immediately before complete failure at 8.8 mm of crosshead displacement; (c) the triangular lattice structure at 7.1 mm of crosshead displacement after a local failure occurred in one small strut (circled); (d) the triangular lattice structure at 10.2 mm of crosshead displacement after a local buckling failure had occurred (circled); (e) the filled triangular lattice structure at 8 mm of crosshead displacement after an initial local buckling failure had occurred (circled); (f) the filled triangular lattice structure at 9.2 mm of crosshead displacement after the local failure of two small struts (circled)

8. Conclusion

Advances in additive manufacturing are shifting the focus of structural optimization from the macrostructure layout to a new paradigm that is capable of incorporating the details of the microstructure. Given this paradigm shift, a systematic algorithm based on Fourier series expansion was created to generate spatially-varying, periodic cellular microstructures that are tailored to attain the optimized performance of the macrostructure. The homogenized properties were validated experimentally, and it was shown that the assumptions of homogenization theory, in which the unit cell must be significantly smaller than the macrostructure, were not restrictive to the macro cellular solid designs that were obtained. The topology and morphology were optimized using homogenization-based topology optimization subjected to multiple load cases. The foci were then placed on the calculation of the amplitude and the phase spectrum of the Fourier series expansion that represented the unit cell lattice and on how the amplitude and updated phase spectrum that was based on the optimized orientation were utilized to project the optimized material distribution to cellular solids. The specific stiffness of the optimized structure with three lattice types with two periodicities was compared, and it was shown that, while reducing periodicity increases the structural performance, the limitations in the precision of the manufacturing may outweigh the increases in stiffness, resulting in lower specific stiffness. It also was shown that, for the single load case designs in which the walls of the cells are aligned with the load paths, squares with rectangular hole lattices with their orthotropic properties can provide the most efficient design. However, the triangular lattices produced cellular solids that were capable of transferring shear, so they may be better used in situations in which there is a large number of load cases. The experimental evaluations of the optimized cellular solids were compared with those obtained using SIMP, and it was shown that both higher stiffness and significantly improved ultimate strength were attained due to the redundant load paths created by the lattices.

Data availability

The data that support the findings of this study are available on request from the corresponding author, AYT.

Credit author statement

A. Tamijani: Conceptualization, Methodology, Development of Optimization Framework, Visualization, Writing. S. P. Velasco: Projection and Post-processing of Homogenized Designs, Visualization, Writing. L. Alacoque: Computational and Experimental Evaluation of Designs, Visualization, Writing.

Declaration of Competing Interest

The authors declare that they have no known competing financial interests or personal relationships that could have appeared to influence the work reported in this paper.

Acknowledgments

The authors gratefully acknowledge the support of the National Science Foundation (NSF) under award number 1847133 with program manager Dr. Kathryn Jablokow. The authors also thank Dr. Marwan Al-Haik for the help he provided for the experimental evaluations of the optimized design. Also, the authors are thankful to Dr. Krister Svanberg for providing the MATLAB GCMMA code.

References

[1] L.J. Gibson, M.F. Ashby, Cellular Solids: Structure and Properties, Cambridge University Press, 1999.
[2] A. Nazir, K.M. Abate, A. Kumar, J.-Y. Jeng, A state-of-the-art review on types, design, optimization, and additive manufacturing of cellular structures, Int. J. Adv. Manuf. Technol. 104 (9–12) (2019) 3489–3510.
[3] P. Zhang, J. Toman, Y. Yu, E. Biyikli, M. Kirca, M. Chmielus, To, A. C, Efficient design-optimization of variable-density hexagonal cellular structure by additive manufacturing: theory and validation, J. Manuf. Sci. Eng. 137 (2) (2015), 021004.
[4] G. Savio, S. Rosso, R. Meneghello, G. Concheri, Geometric modeling of cellular materials for additive manufacturing in biomedical field: a review, Appl. Bionics Biomech. Vol. 2018 (2018).
[5] J. Tian, T.J. Lu, H.P. Hodson, D.T. Queheillalt, H.N.G. Wadley, Cross flow heat exchange of textile cellular metal core sandwich panels, Int. J. Heat Mass Transf. 50 (13) (2007) 2521–2536.
[6] I. Maskery, N.T. Aboulkhair, A.O. Aremu, C.J. Tuck, I.A. Ashcroft, Compressive failure modes and energy absorption in additively manufactured double gyroid lattices, Addit. Manufact. 16 (2017) 24–29.
[7] X. Wang, T.J. Lu, Optimized acoustic properties of cellular solids, J. Acoustical Soc. Am. 106 (2) (1999) 756–765.
[8] G. Allaire, Shape Optimization by the Homogenization Method, Springer Science & Business Media, 2012.
[9] R.V. Kohn, G. Strang, Optimal design and relaxation of variational problems, III, Commun. Pure Appl. Math. 39 (3) (1986) 353–377.
[10] M.P. Bendsoe, N. Kikuchi, Generating optimal topologies in structural design using a homogenization method, Comput. Methods Appl. Mech. Eng. 71 (2) (1988) 197–224.
[11] P. Pedersen, On optimal orientation of orthotropic materials, Struct. Multidiscip. Optim. 1 (2) (1989) 101–106.
[12] H. Cheng, N. Kikuchi, Z. Ma, An improved approach for determining the optimal orientation of orthotropic material, Struct. Multidiscip. Optim. 8 (2) (1994) 101–112.
[13] H. Rodrigues, J.M. Guedes, M.P. Bendsoe, Hierarchical optimization of material and structure, Struct. Multidiscip. Optim. 24 (1) (2002) 1–10.
[14] J. Gao, Z. Luo, H. Li, Gao, L. J. C. M. I. A. M., and Engineering, Topology optimization for multiscale design of porous composites with multi-domain microstructures, Vol. 344, 2019 451–476.
[15] Y. Zhang, M. Xiao, X. Zhang, L. Gao, Topological design of sandwich structures with graded cellular cores by multiscale optimization, Comput. Methods Appl. Mech. Eng. 361 (2020) 112749.
[16] O. Pantz, K. Trabelsi, A post-treatment of the homogenization method for shape optimization, SIAM J. Control. Optim. 47 (3) (2008) 1380–1398.
[17] J.P. Groen, O. Sigmund, Homogenization-based topology optimization for high-resolution manufacturable micro-structures, Int. J. Numer. Methods Eng. 113 (8) (2017) 1148–1163.
[18] G. Allaire, P. Geoffroy-Donders, O. Pantz, Topology optimization of modulated and oriented periodic microstructures by the homogenization method, Comput. Math. Appl. 78 (7) (2019) 2197–2229.
[19] M. Maldovan, E.L. Thomas, Periodic materials and interference lithography: for photonics, phononics and mechanics, John Wiley & Sons, 2009.
[20] R.C. Rumpf, J. Pazos, Synthesis of spatially variant lattices, Opt. Express 20 (14) (2012) 15263–15274.
[21] J. Guedes, N. Kikuchi, Preprocessing and postprocessing for materials based on the homogenization method with adaptive finite element methods, Comput. Methods Appl. Mech. Eng. 83 (2) (1990) 143–198.
[22] B. Hassani, E. Hinton, A review of homogenization and topology optimization I—homogenization theory for media with periodic structure, Comput. Struct. 69 (6) (1998) 707–717.
[23] E. Andreassen, C.S. Andreasen, How to determine composite material properties using numerical homogenization, Comput. Mater. Sci. 83 (2014) 488–495.
[24] I. Maskery, L. Sturm, A. Aremu, A. Panesar, C. Williams, C. Tuck, R.D. Wildman, I. Ashcroft, R.J. Hague, Insights into the mechanical properties of several triply periodic minimal surface lattice structures made by polymer additive manufacturing, Polymer 152 (2017) 62–71.
[25] K. Svanberg, MMA and GCMMA - Two Methods for Nonlinear Optimization, 2007.
[26] H. Gea, J. Luo, On the stress-based and strain-based methods for predicting optimal orientation of orthotropic materials, Struct. Multidiscip. Optim. 26 (3) (2004) 229–234.
[27] J.P. Groen, F.C. Stutz, N. Aage, J.A. Bærentzen, O. Sigmund, De-homogenization of optimal multi-scale 3D topologies, Comput. Methods Appl. Mech. Eng. 364 (2020) 112979.
[28] P. Wesseling, Principles of Computational Fluid Dynamics, Springer Science & Business Media, 2009.
[29] A.Y. Tamijani, J. Hurley, K. Gharibi, Determination of load paths in plates and shells, Thin-Walled Struct. 127 (2018) 646–653.
[30] A.Y. Tamijani, K. Gharibi, M.H. Kobayashi, R.M. Kolonay, Load paths visualization in plane elasticity using load function method, Int. J. Solids Struct. 135 (2018) 99–109.
[31] Y. Tong, S. Lombeyda, A.N. Hirani, M. Desbrun, Discrete multiscale vector field decomposition, ACM Transactions on Graphics (TOG), Vol. 22, ACM 2003, pp. 445–452.
[32] X. Zheng, B. Parlett, A. Pang, Topological structures of 3D tensor fields, Visualization, 2005. *VIS 05*. IEEE, IEEE 2005, pp. 551–558.
[33] I. Hotz, J. Sreevalsan-Nair, H. Hagen, B. Hamann, Tensor field reconstruction based on eigenvector and eigenvalue interpolation, Dagstuhl Follow-Ups, Vol. 1, Schloss Dagstuhl-Leibniz-Zentrum fuer Informatik, 2010.